Science Advances
AAAS

Supplementary Materials for

Highly-integrated, miniaturized, stretchable electronic systems based on stacked multilayer network materials

Honglie Song, Guoquan Luo, Ziyao Ji, Renheng Bo, Zhaoguo Xue, Dongjia Yan, Fan Zhang, Ke Bai, Jianxing Liu, Xu Cheng, Wenbo Pang, Zhangming Shen, Yihui Zhang*

*Corresponding author. Email: yihuizhang@tsinghua.edu.cn

Published 16 March 2022, *Sci. Adv.* **8**, eabm3785 (2022)
DOI: 10.1126/sciadv.abm3785

The PDF file includes:

Other Supplementary Material for this manuscript includes the following:

Note S1. Assembly procedure for the multilayer device system.

The assembly procedure of the multilayer device system is illustrated in the fig. S38C. We first place the 1st circuit layer (including the PI network materials and circuit) with a PDMS stamp onto a bottom glass slide, and then use another PDMS stamp with strategic holes to transfer the 2nd circuit layer (including the PI network materials and circuit) onto the 1st circuit layer (fig. S38C). During the alignment, the 2nd PI network is in contact with the individual components of the 1st circuit layer. Then we remove the top glass slide, and connect the vias of the 1st and the 2nd circuit layers by silver pillars, through the holes of the top PDMS stamp. Soldering the silver pillars to the vias and removing the top PDMS stamps completes the assembly of the 1st and the 2nd circuit layers. Repeating this process allows the assembly of the entire multilayer device system (fig. S39).

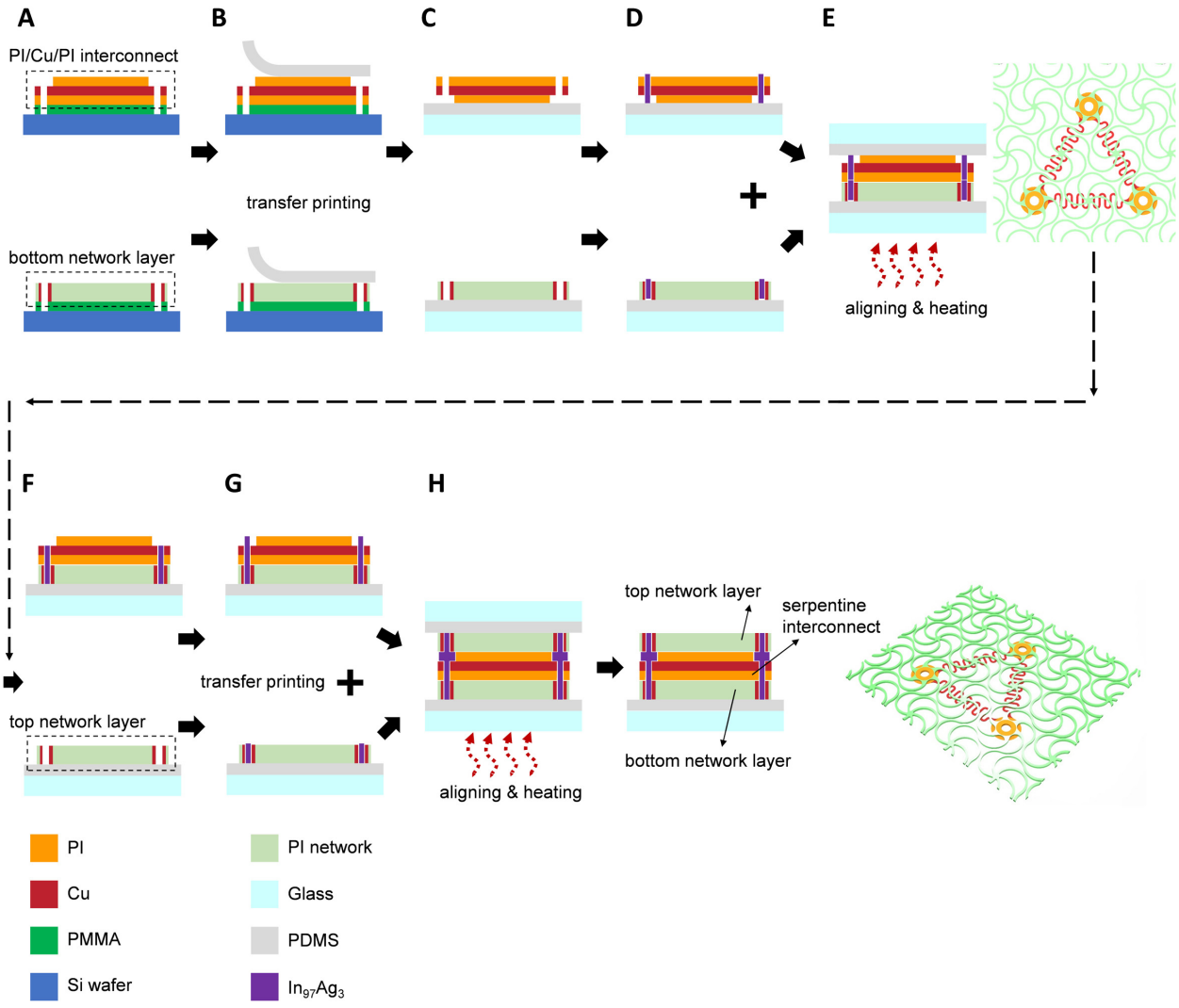

fig. S1. Schematic illustration of the fabrication process of stretchable interconnects encapsulated by bilayer network materials. (**A**)-(**D**) Transfer printing of the serpentine interconnects and the bottom network layer. (**E**) Aligning the transfer printed serpentine interconnect and bottom network layer, and then soldering them together. (**F**) & (**G**) Transfer printing of the top network layer. (**H**) Aligning and soldering to obtain the stacked bilayer network materials with encapsulated serpentine interconnect.

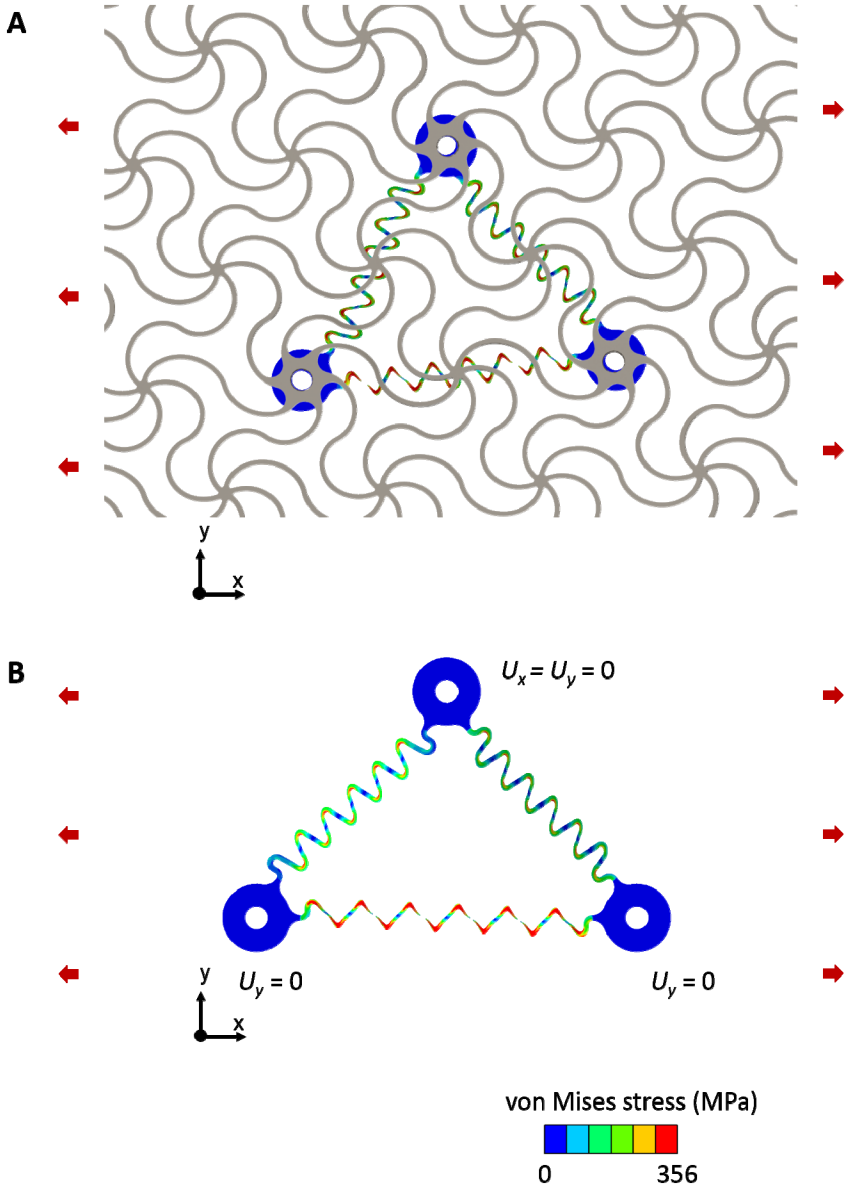

fig. S2. FEA results for the deformed configuration of encapsulated serpentine interconnects at the elastic limit, in comparison to the case of freestanding serpentine interconnects in fig. 1A. The color of serpentine interconnects represents the magnitude of von Mises stress in the metal layer. (**A**) Deformed configuration of serpentine interconnects encapsulated by bilayer network materials at the elastic limit (37%). (**B**) Deformed configuration of freestanding serpentine interconnects at the elastic limit (46%).

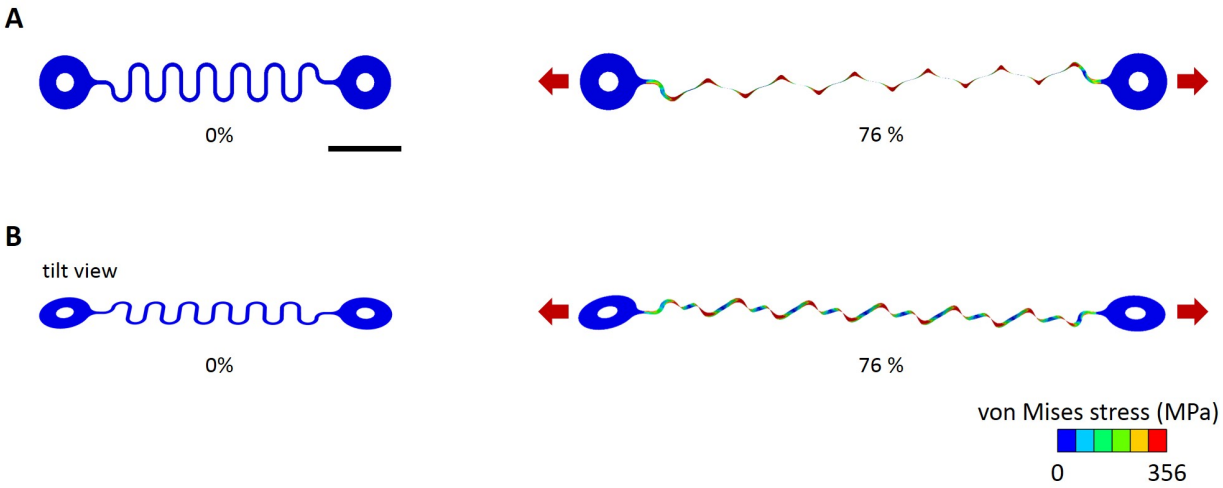

fig. S3. FEA results for the deformed configuration of the serpentine interconnect (in Fig. 1B and C) in the freestanding condition. (**A**) Top view of the serpentine interconnect when uniaxially stretched to its elastic stretchability (76%). (**B**) Tilt view of the serpentine interconnect. The color of serpentine interconnects represents the magnitude of von Mises stress in the metal layer. Scale bar, 1 mm.

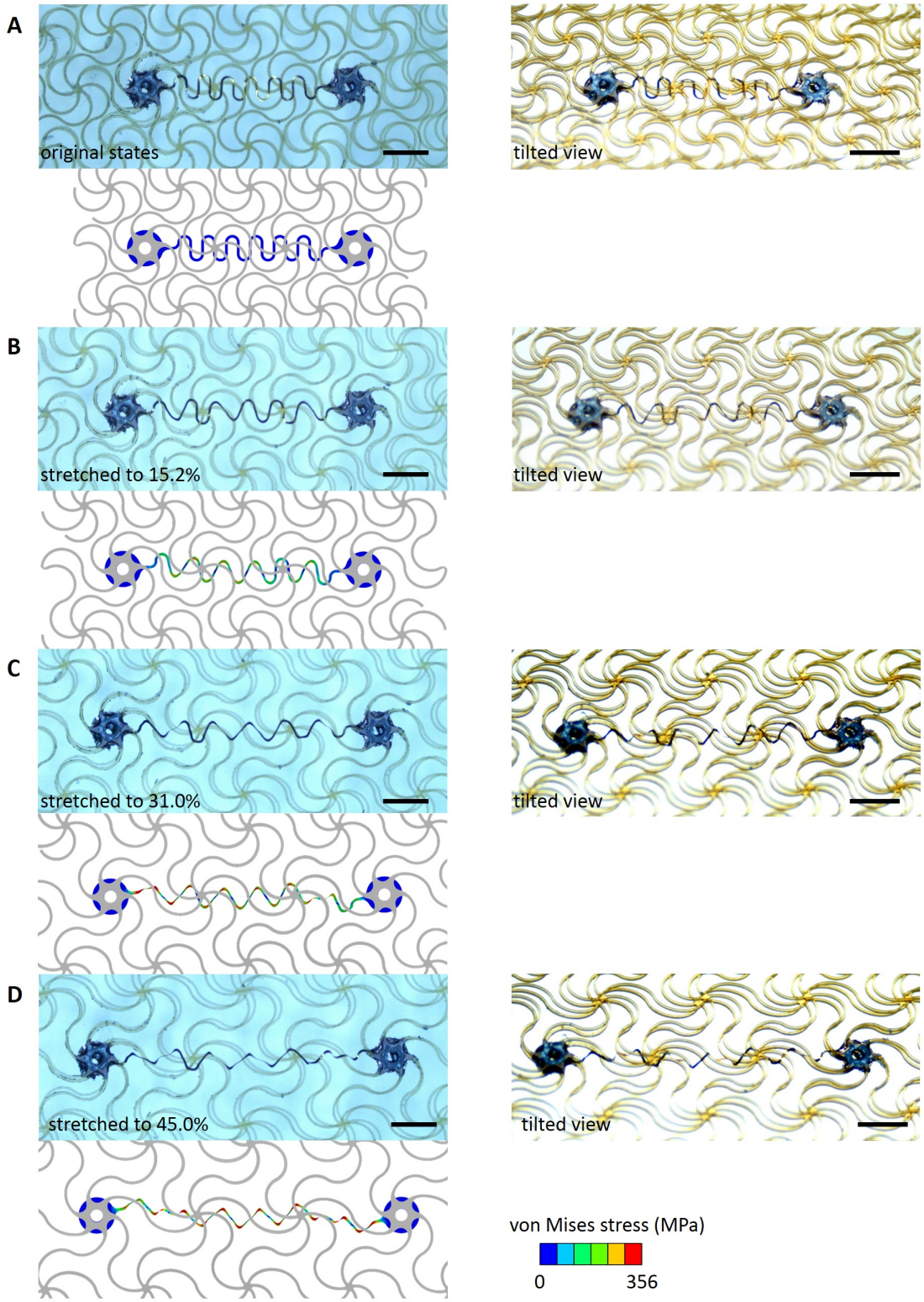

fig. S4. Optical images (top) and FEA results (bottom) of the serpentine interconnects encapsulated by bilayer network materials, during the uniaxial stretching, until reaching its elastic stretchability (45%). The color of serpentine interconnects represents the magnitude of von Mises stress in the metal layer.Scale bars, 1 mm.

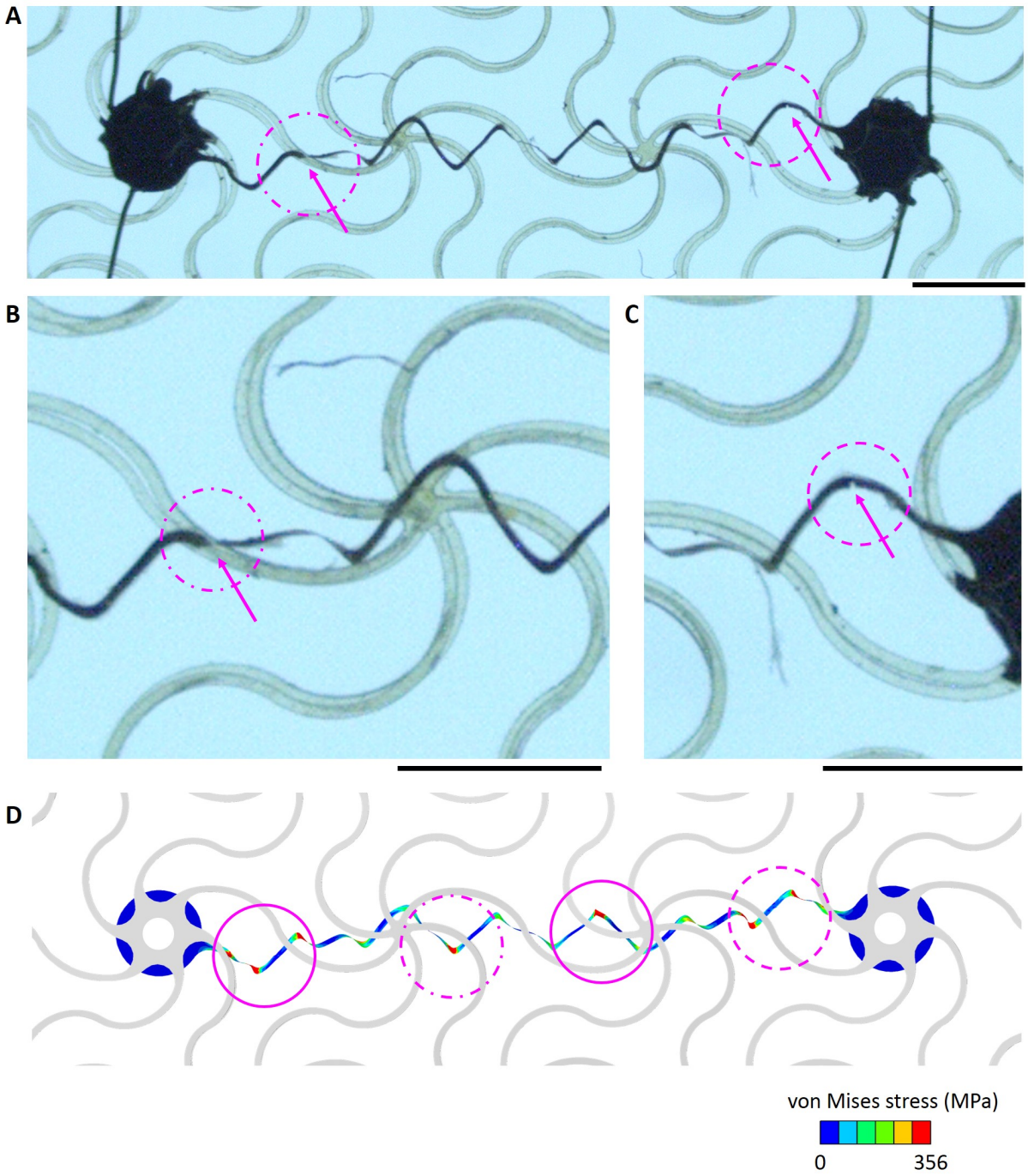

fig. S5. Optical images that show the sites of fatigue fracture in the serpentine interconnects encapsulated by bilayer network materials, after the tensile cycling test. (**A**)-(**C**) Global and enlarged views showing that the copper layer of the interconnects breaks before the polyimide layer. (**D**) FEA results on the distribution of von Mises stress in the metal layer for the encapsulated serpentine interconnect under uniaxial stretching. The sites of maximum von Mises stress in the metal layer are in accordance with the sites of fatigue fracture. Scale bars, 1 mm.

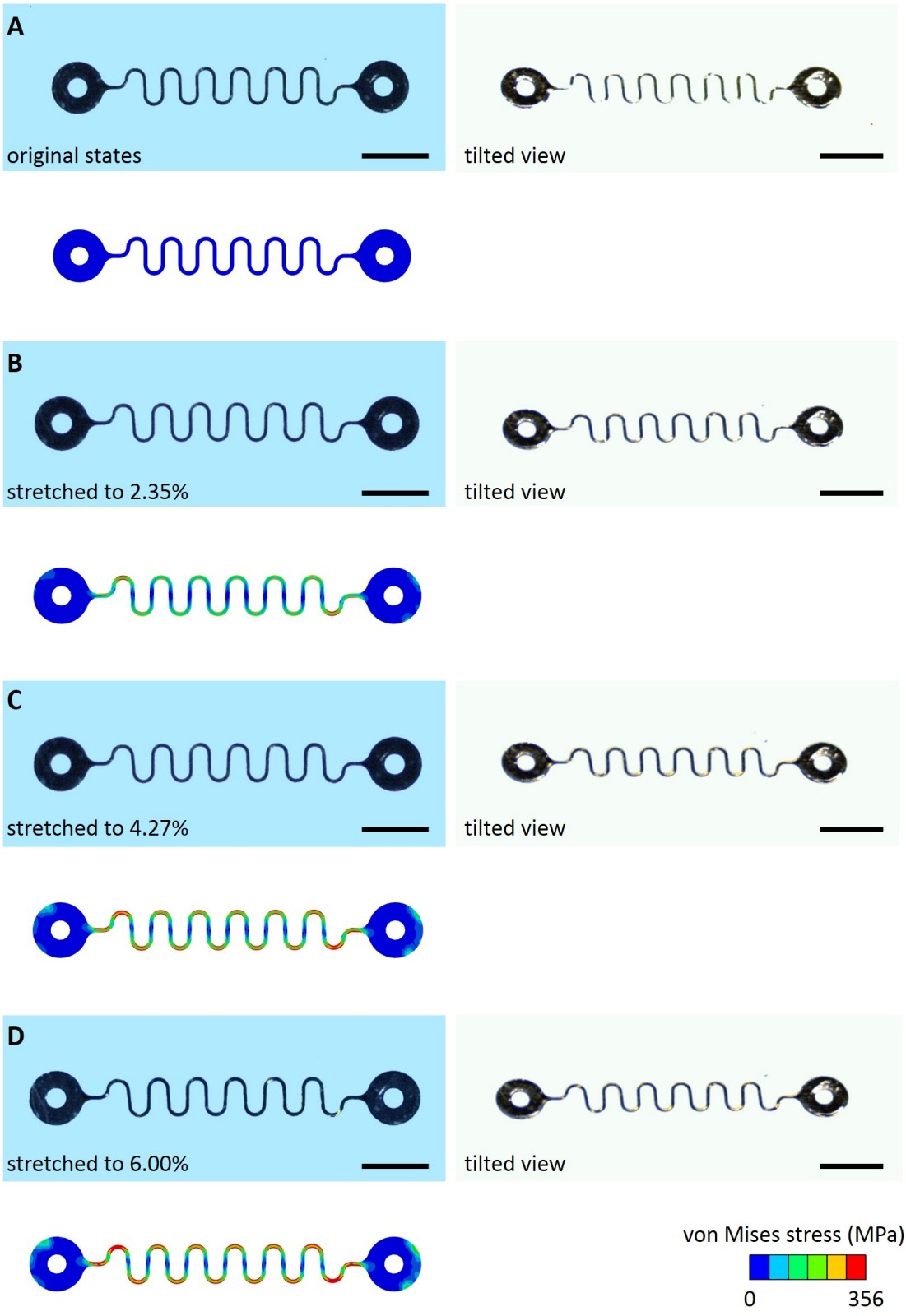

fig. S6. Optical images (top) and FEA results (bottom) for the serpentine interconnects encapsulated by PDMS, during the uniaxial stretching. The color of serpentine interconnects represents the magnitude of von Mises stress in the metal layer. Scale bars, 1 mm.

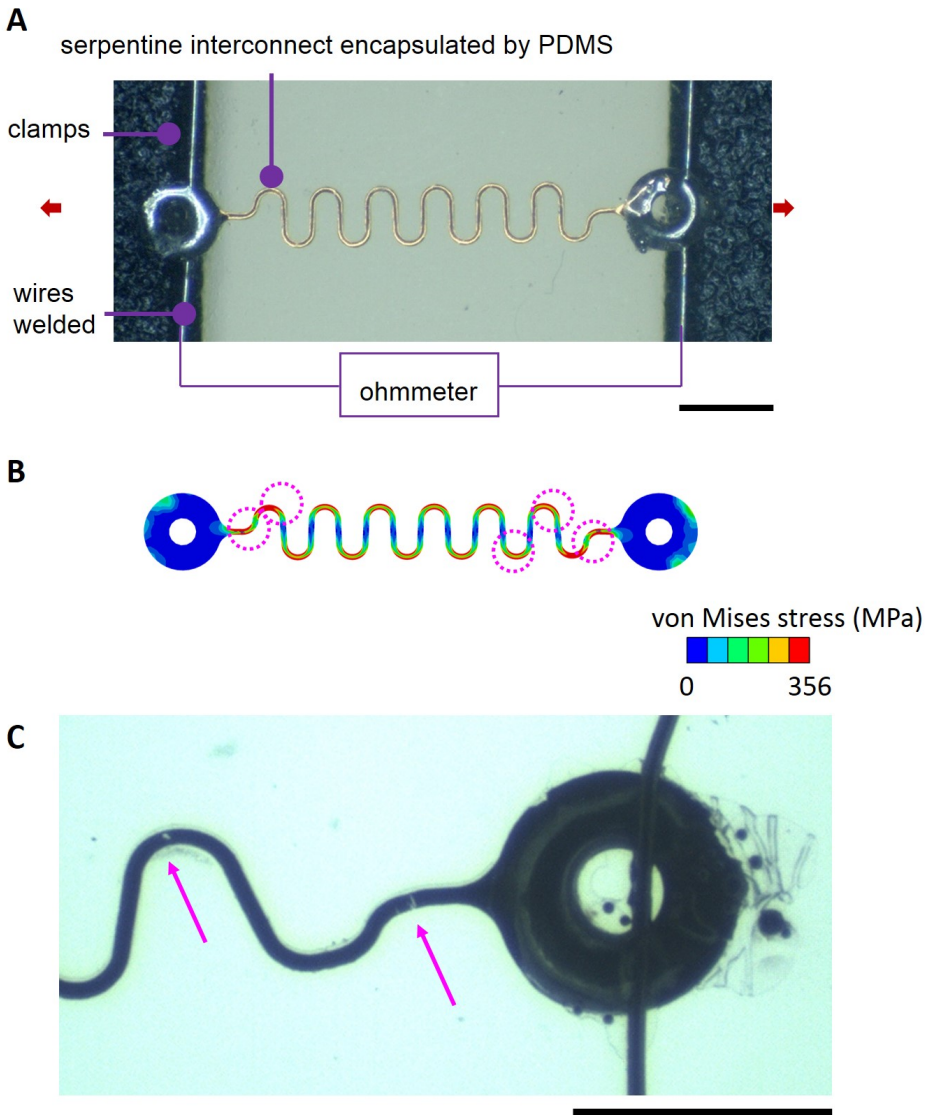

fig. S7. Fatigue tests for encapsulated interconnects under cyclic uniaxial stretching. (**A**) Experimental detail of the fatigue test. (**B**) FEA results of the deformed serpentine interconnect encapsulated by PDMS, under 6% uniaxial stretching. The color of serpentine interconnects represents the magnitude of von Mises stress in the metal layer. The black color corresponds to the regions that the von Mises stress reaches the yield limit (356 MPa) at the top or bottom surfaces. (**C**) Sites of fatigue fracture in the serpentine interconnects encapsulated by PDMS, after the cyclic tension. Scale bars, 1 mm.

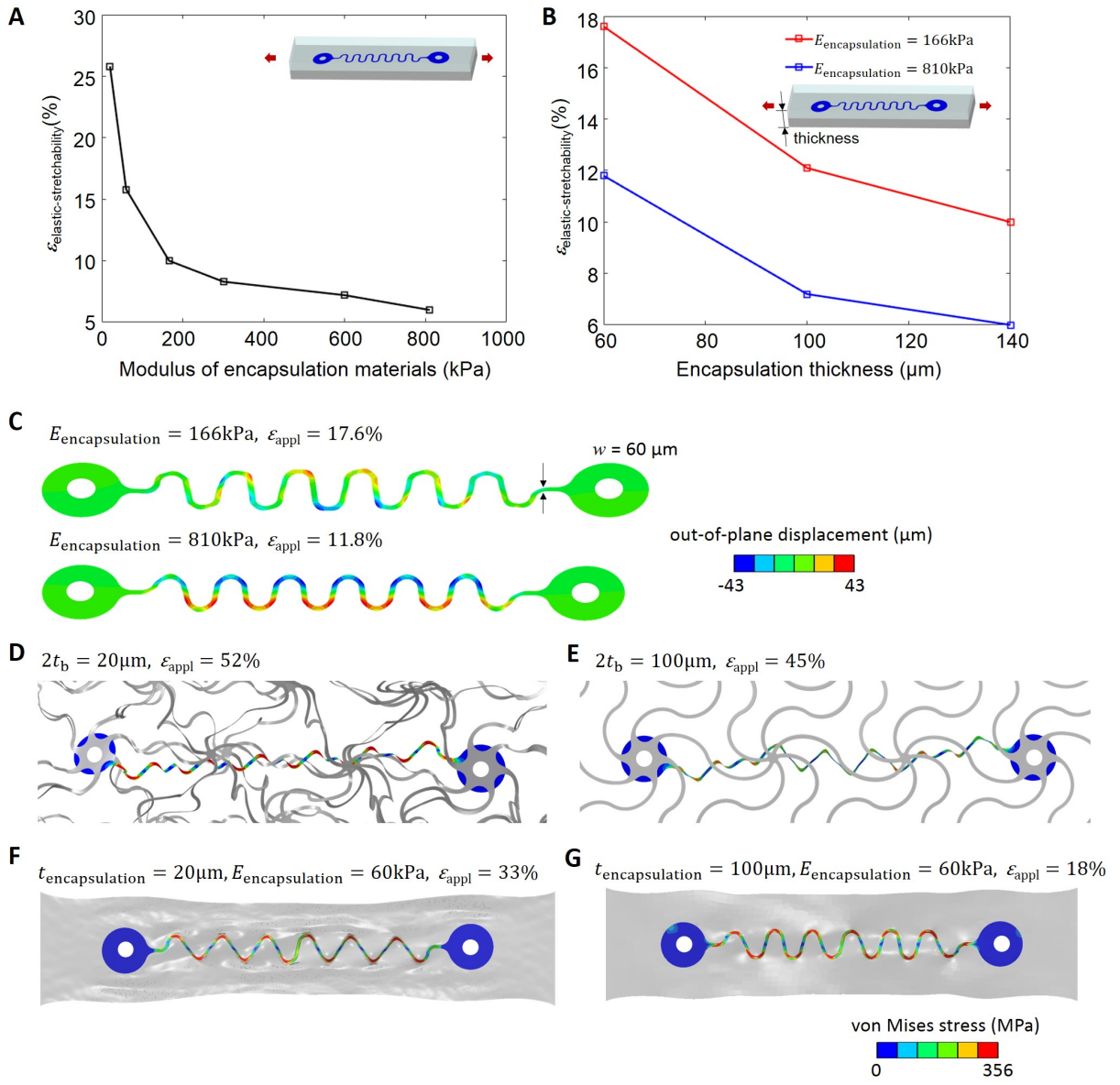

fig. S8. Effects of the elastic modulus of the encapsulation material (A) and the thickness of the encapsulation layer (B) on the elastic stretchability of serpentine interconnects in the solid encapsulation strategy. (**C**) Out-of-plane displacement of the interconnect encapsulated by a 60 μm thick elastomer with elastic moduli 166 kPa and 810 kPa, respectively. The interconnects are stretched to their elastic limit. (**D**)-(**E**) von Mises stress distribution of the interconnect encapsulated by SMNM. The total thickness of the bilayer network is 20 μm in (**D**) and 100 μm in (**E**). Other design parameters are same as those in fig. 1B. The interconnects are stretched to their elastic limits. (**F**)-(**G**) von Mises stress distribution of the interconnect encapsulated by soft elastomer with a modulus of 60 kPa. The thickness of the elastomer is 20 μm in (**F**) and 100 μm in (**G**). The interconnects are stretched to their elastic limits.

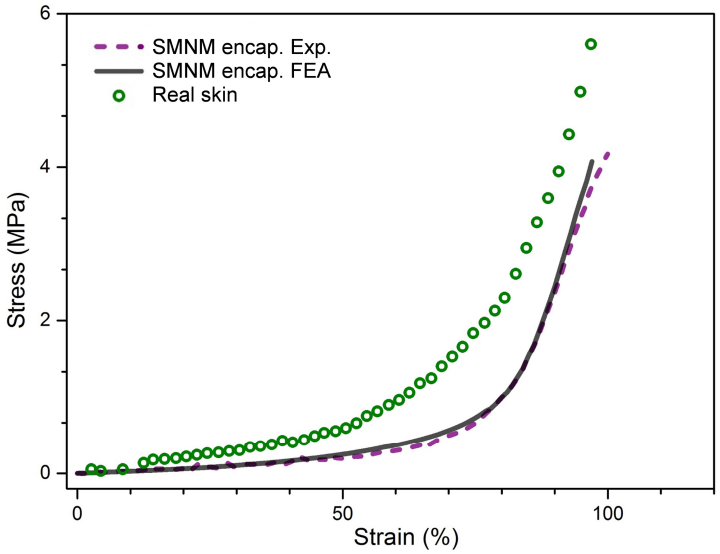

fig. S9. Stress-strain responses of bilayer PI networks with encapsulated serpentine interconnects, in comparison to that of human skin at the abdomen region. The FEA and experimental data are denoted by the solid line and dashed line, respectively, while the experimental results of human skin are denoted by circles [64].

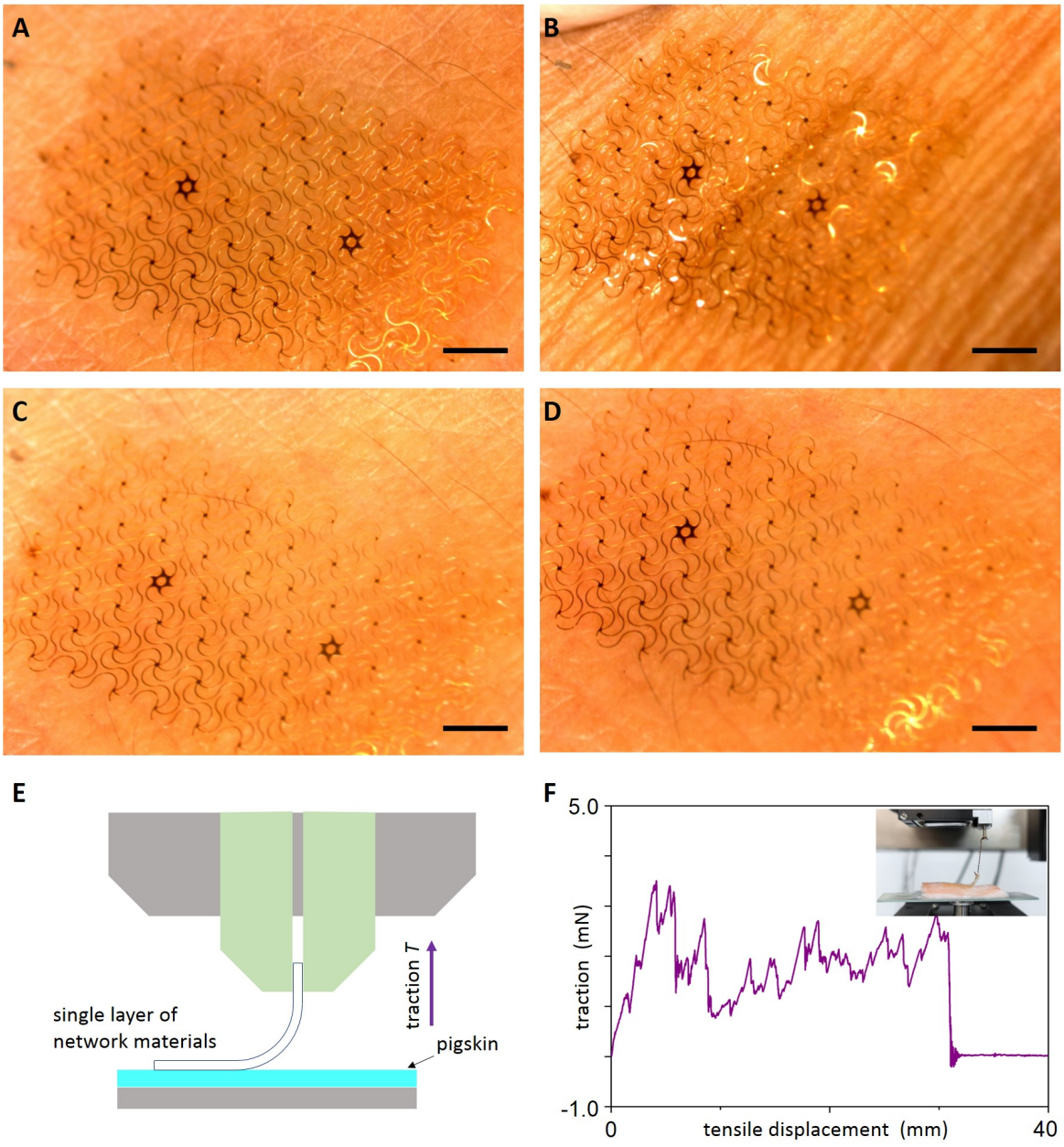

fig. S10. Optical images of the network materials mounted on the skin. (**A**) A layer of PI network material with a thin coating of the medical Vaseline can be attached coherently with the human skin. (**B**) Deformed states under compressing (**B**), stretching (**C**), and shearing (**D**). (**E**) Schematic illustration of peeling test, and (**F**) plot of the traction versus tensile displacement on the pigskin. The network sample has a length of 15.7 mm and a width of 8.9 mm. Scale bars, 0.5 mm.

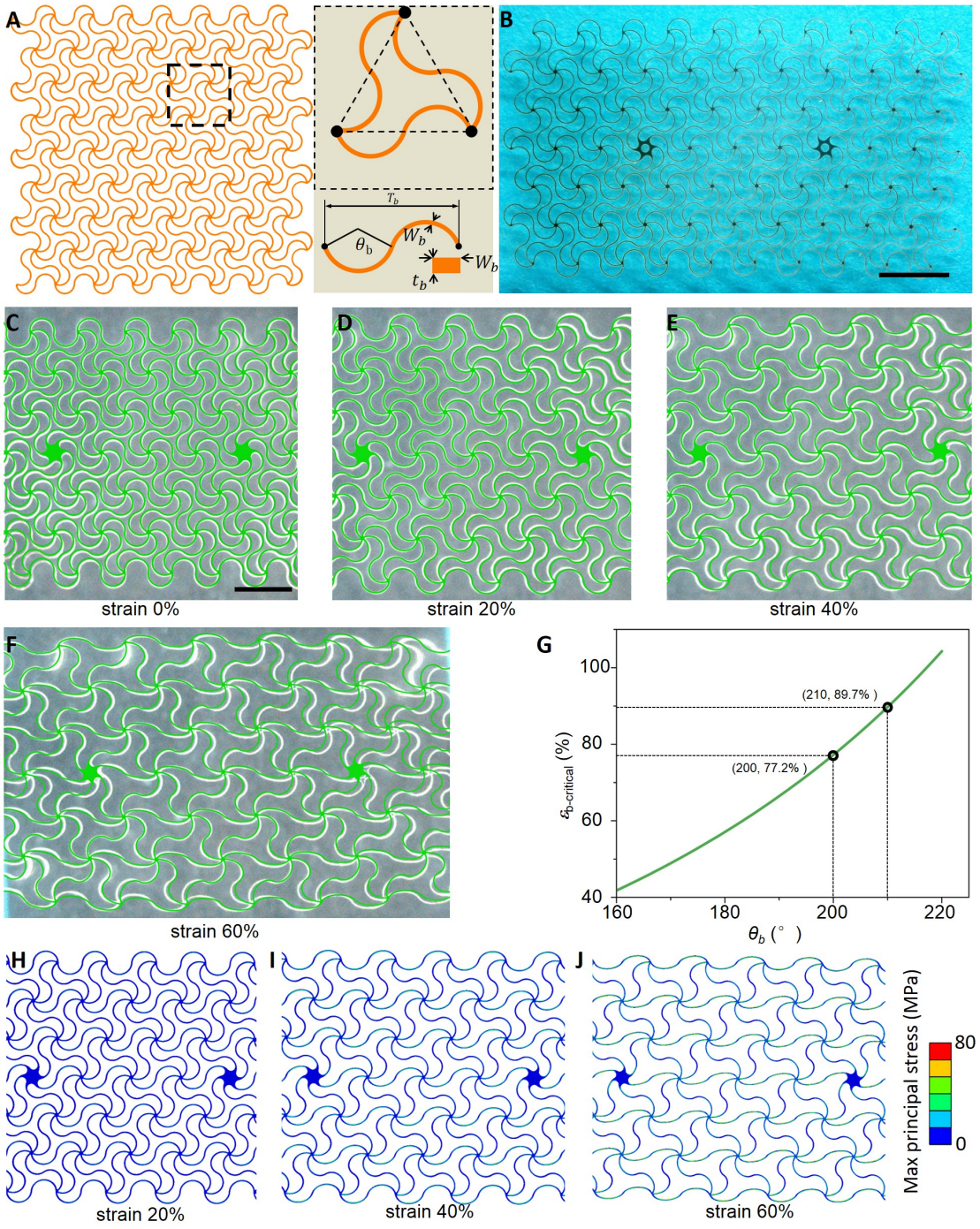

fig. S11. FEA results on the deformed configurations of a single-layer network material under uniaxial stretching. (**A**) Illustration of key geometric parameters of the soft network consisting of horseshoe microstructures. (**B**) Optical images of the network. (**C**)-(**F**) FEA results overlaid with optical images of deformed network materials at different levels of uniaxial stretching: (**C**) 0%, (**D**) 20%, (**E**) 40%, and (**F**) 60%. (**G**) Critical strain of the soft network (when the horseshoe microstructures along the loading direction are straightened) versus the arc angle (θ_b) of the horseshoe microstructure. (**H**)-(**J**) FEA result of max principal stress of deformed network materials at different levels of uniaxial stretching: 20%, 40%, and 60%. The color of the network represents the magnitude of max principal stress in the network.

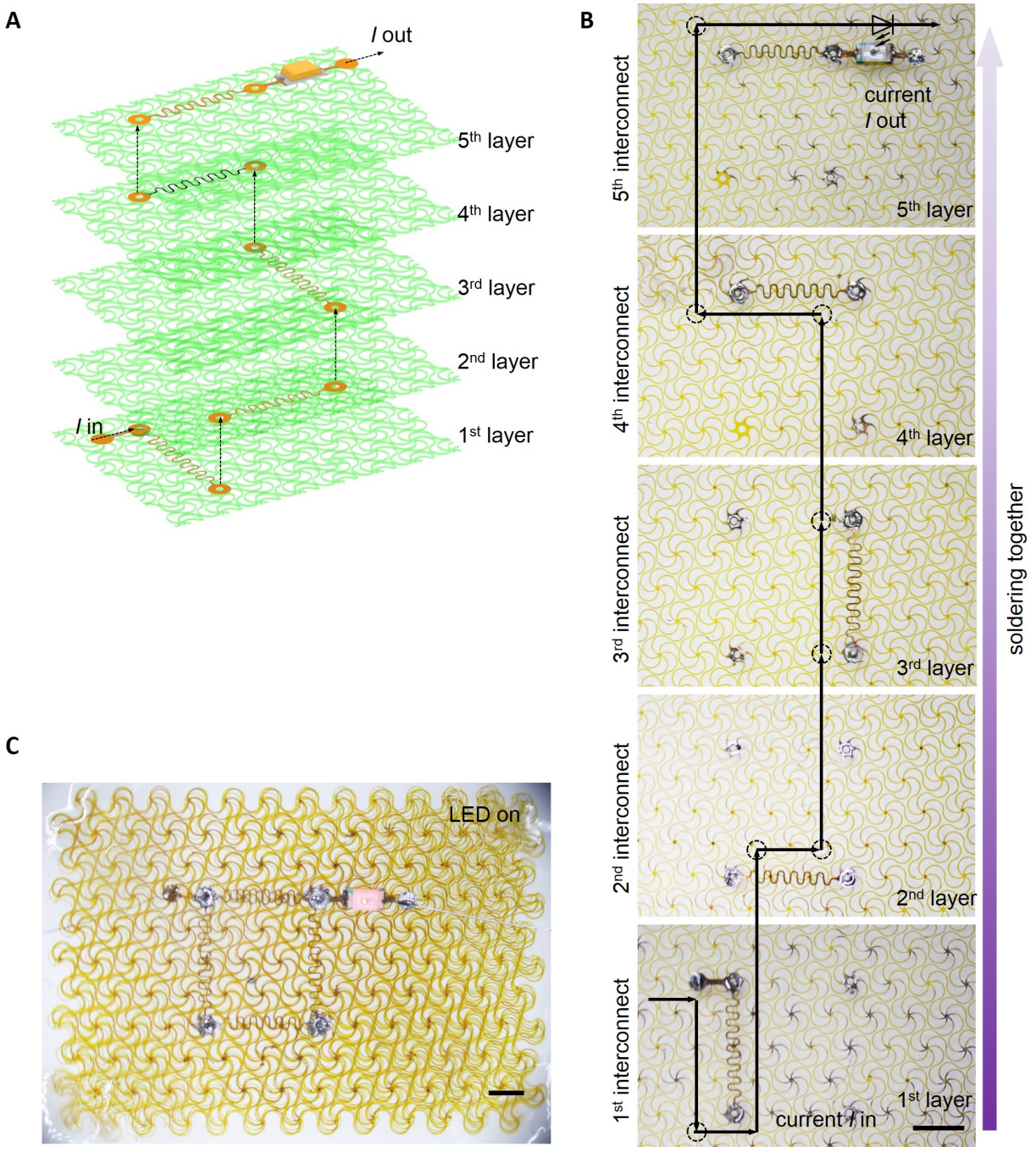

fig. S12. Schematic illustration for the stretchable LED device based on a 5-layer network material. (**A**) Exploded view of the device. (**B**) Illustration of the circuit connection and current flow of the device. (**C**) Details of the stretchable device when the LED is ON. Scale bars, 1 mm.

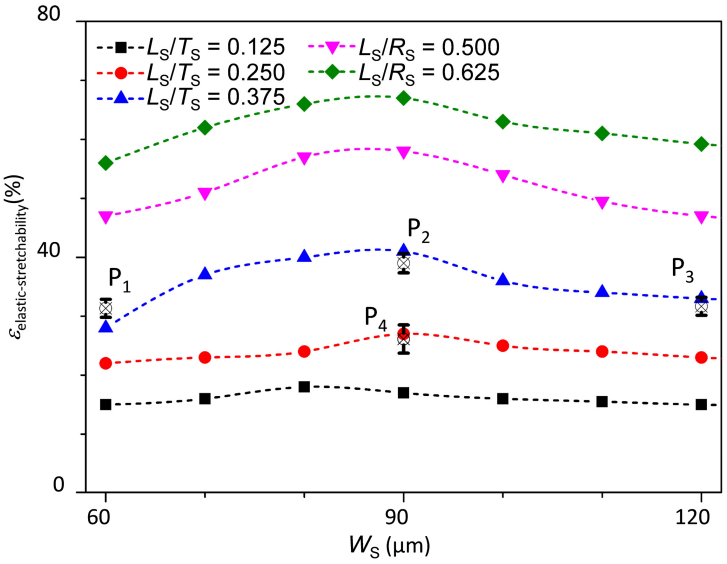

fig. S13. FEA predictions of the elastic stretchability at different interconnect widths and height/spacing ratio, as well as experimental results based on fatigue tests of four representative serpentine interconnects (P_1-P_4 in Fig. 2C).

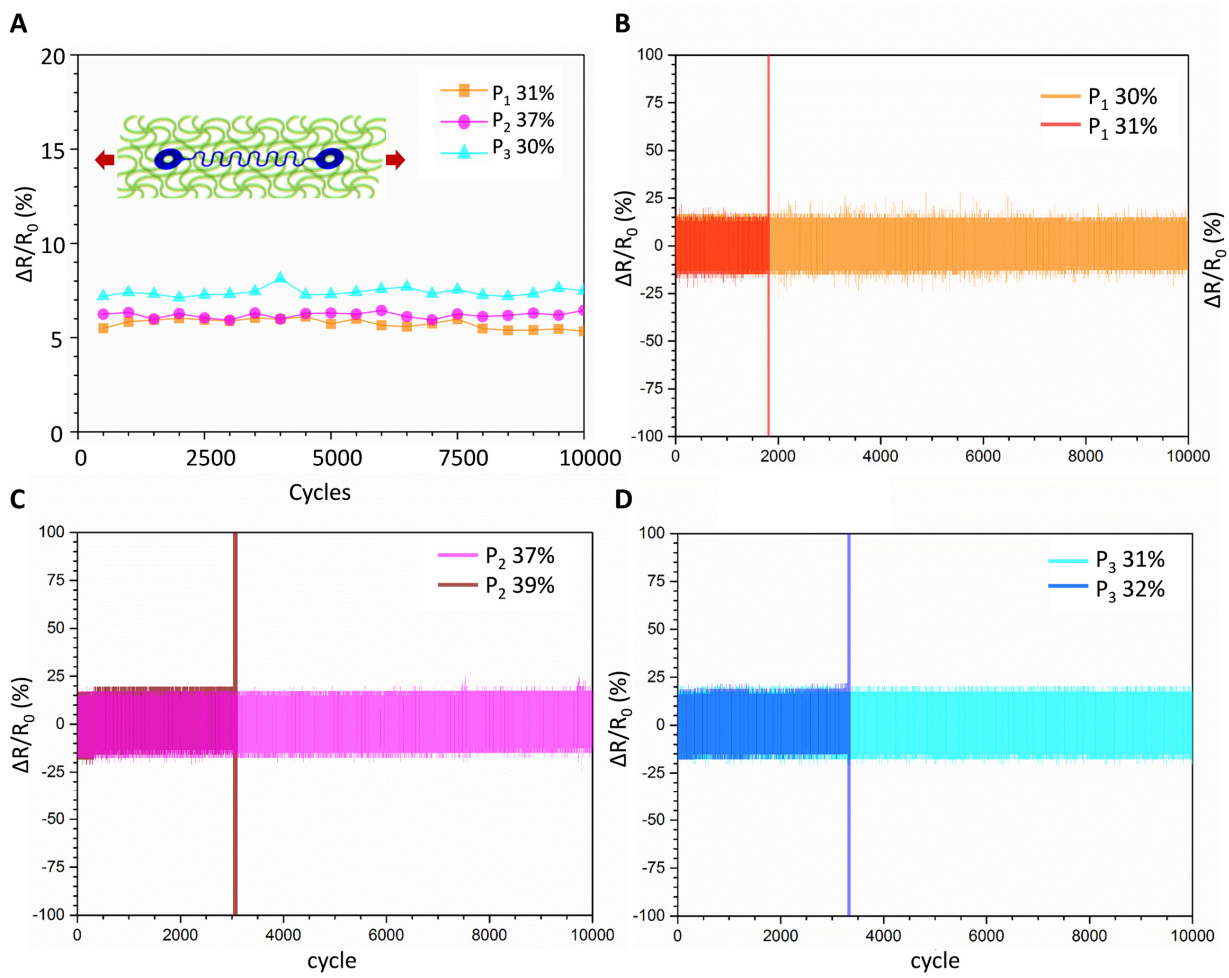

fig. S14. Relative resistance change of serpentine interconnects encapsulated by bilayer network materials, during the cyclic testing. (**A**) Relative change of the resistance (sampling frequency 50 Hz) averaged over 500 cycles. Different levels of uniaxial strain amplitudes (31%, 37%, and 30%) were applied to the designs of P_1, P_2, and P_3 (in Fig. 2C and E) for 10,000 cycles. The relative large variation of the curve for P_3 can be attributed to the thermal fluctuation of the ambient environment over the entire cyclic test (that takes ~ 45 hours). (**B**) Source data of the relative resistance change collected with a sampling frequency of 50 Hz for the design P_1. The interconnect was fractured after ~ 1800 cycles of 31% uniaxial tension. (**C**) Source data of the relative resistance change collected with a sampling frequency of 50 Hz for the design P_2. The interconnect was fractured after ~ 3000 cycles of 39% uniaxial tension. (**D**) Source data of the relative resistance change collected with a sampling frequency of 50 Hz for the design P_3. The interconnect was fractured after ~ 3300 cycles of 32% uniaxial tension.

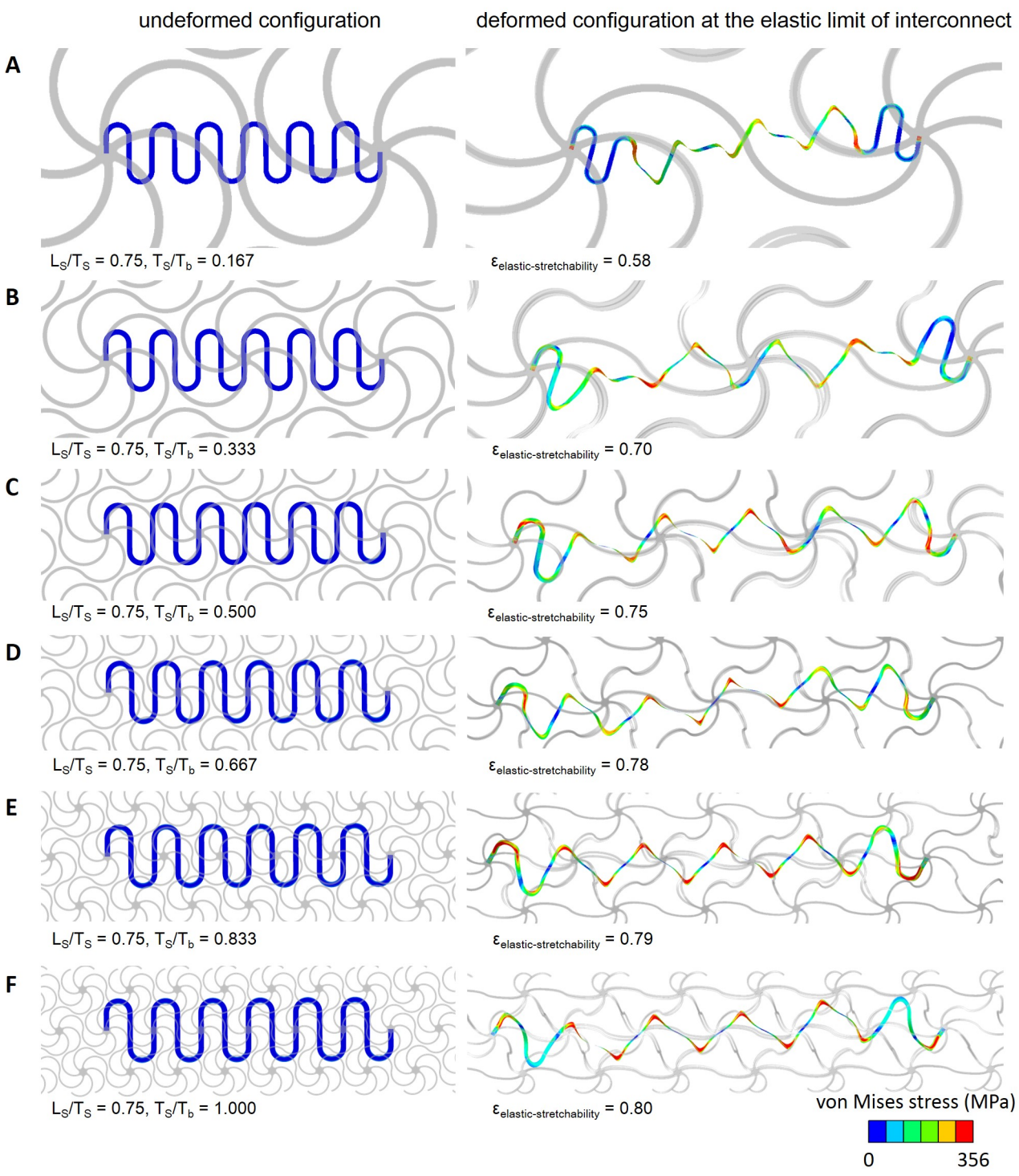

fig. S15. FEA results of deformed configurations for the encapsulated interconnects in fig. 2F and fig. 2G. (**A**)-(**F**) correspond to the design points with geometric parameters (L_s/T_s, T_s/T_b) = (0.75, 0.167), (0.75, 0.333), (0.75, 0.500), (0.75, 0.667), (0.75, 0.833), and (0.75, 1.000). The color of serpentine interconnects represents the magnitude of von Mises stress in the metal layer.

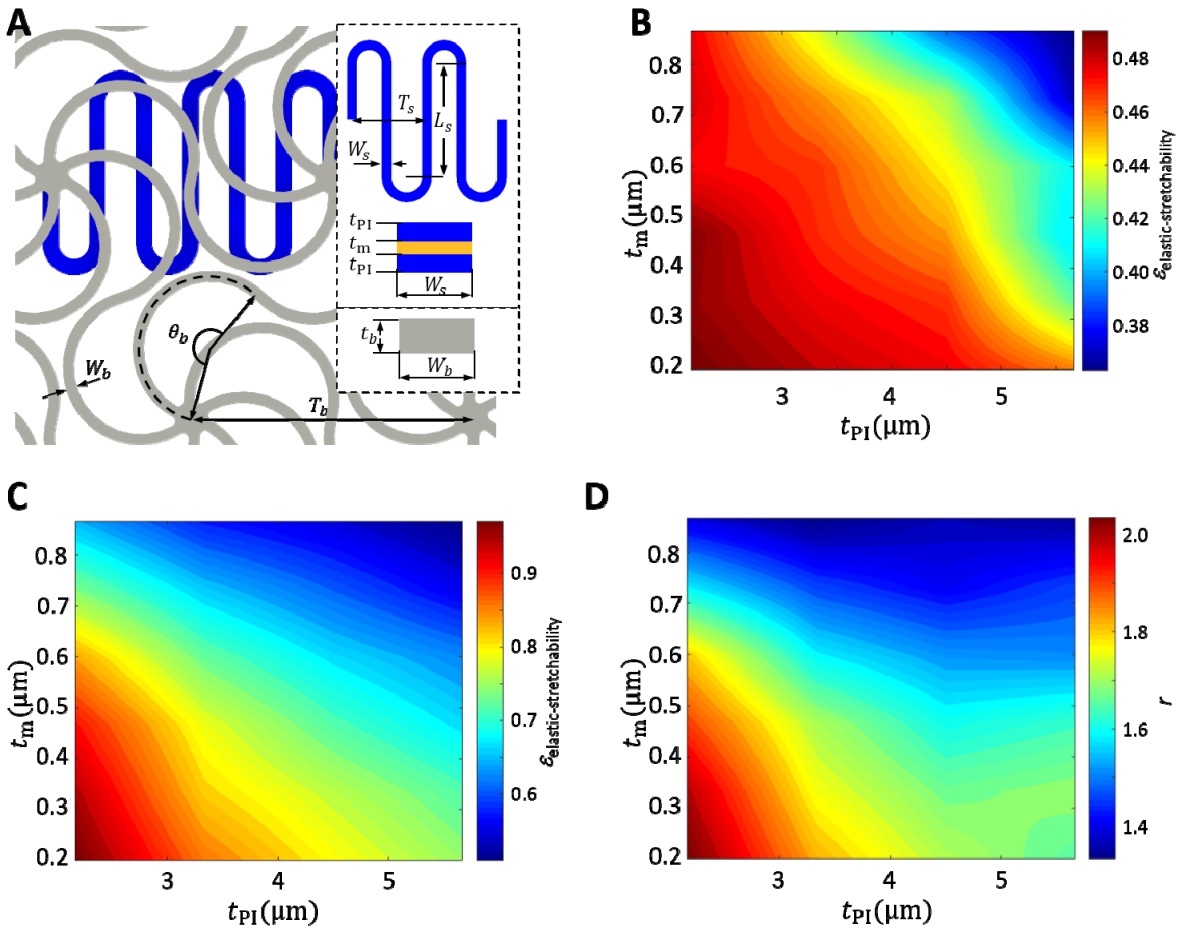

fig. S16. Parametric analysis of the elastic stretchability and constraint factor. (**A**) Illustration of key geometric parameters for a serpentine interconnect encapsulated by two network layers. (**B**) Contour plot of the elastic stretchability of the interconnect encapsulated by two network layers, in terms of the thicknesses t_m and t_{PI}. (**C**) Contour plot of the elastic stretchability of the freestanding interconnect in terms of the thicknesses t_m and t_{PI}. (**D**) Contour plot of the constraint factor. Other geometric parameters include $W_s/T_s = 0.155$, $L_s/T_s = 0.75$, $T_s/T_b = 0.25$, and $T_s = 386.37$ μm.

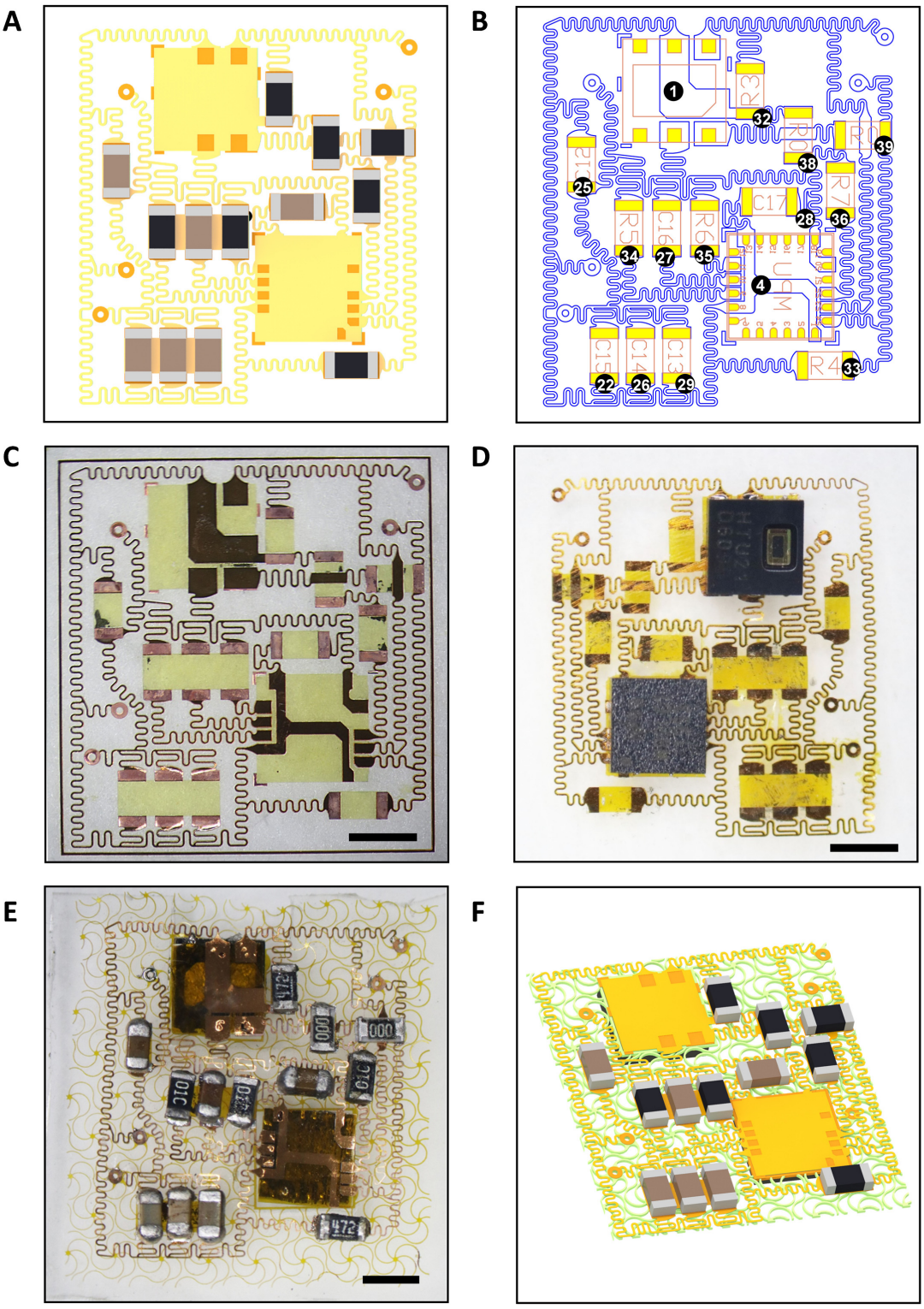

fig. S17. Schematic illustration of the 1st circuit layer, including CAD pattern for the circuit design, PI network materials, and deployment of the individual components. Scale bars, 1 mm.

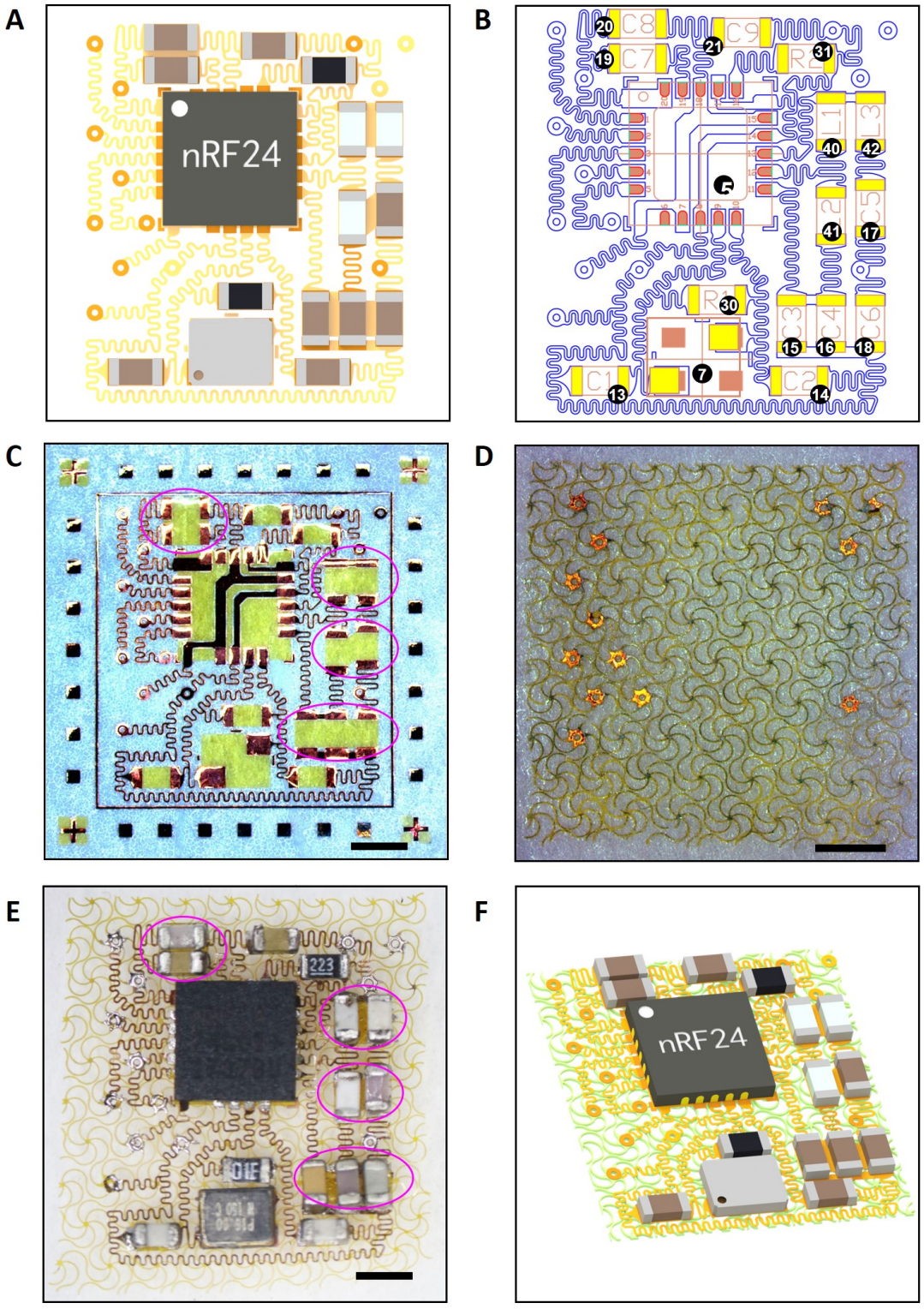

fig. S18. Schematic illustration of the 2nd circuit layer, including CAD pattern for the circuit design, PI network materials, and deployment of the individual components. The circles in C, E noted the PI island design for isolation of adjacent ICs. Scale bars, 1 mm.

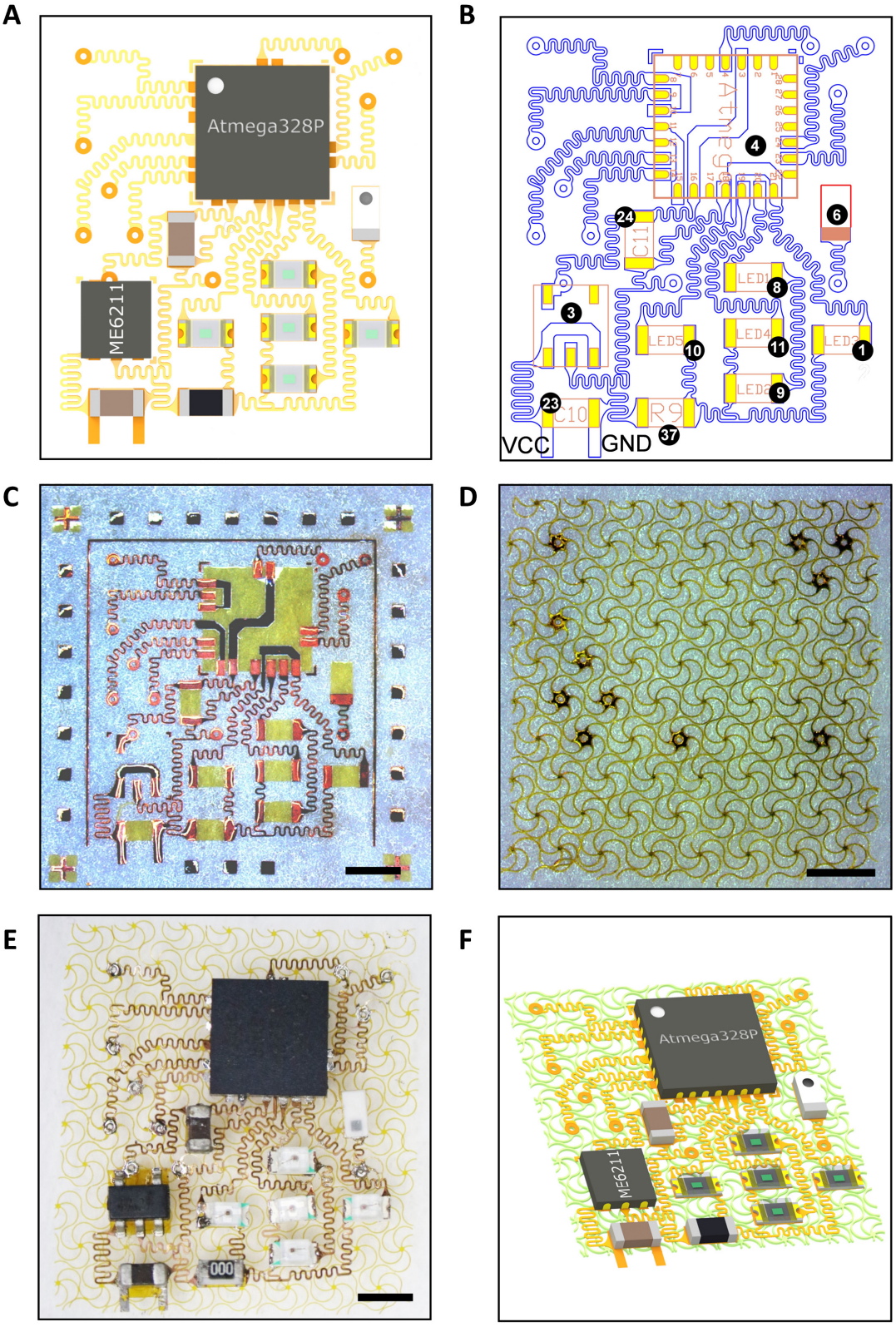

fig. S19. Schematic illustration of the 3rd circuit layer, including CAD pattern for the circuit design, PI network materials, and deployment of the individual components. Scale bars, 1 mm.

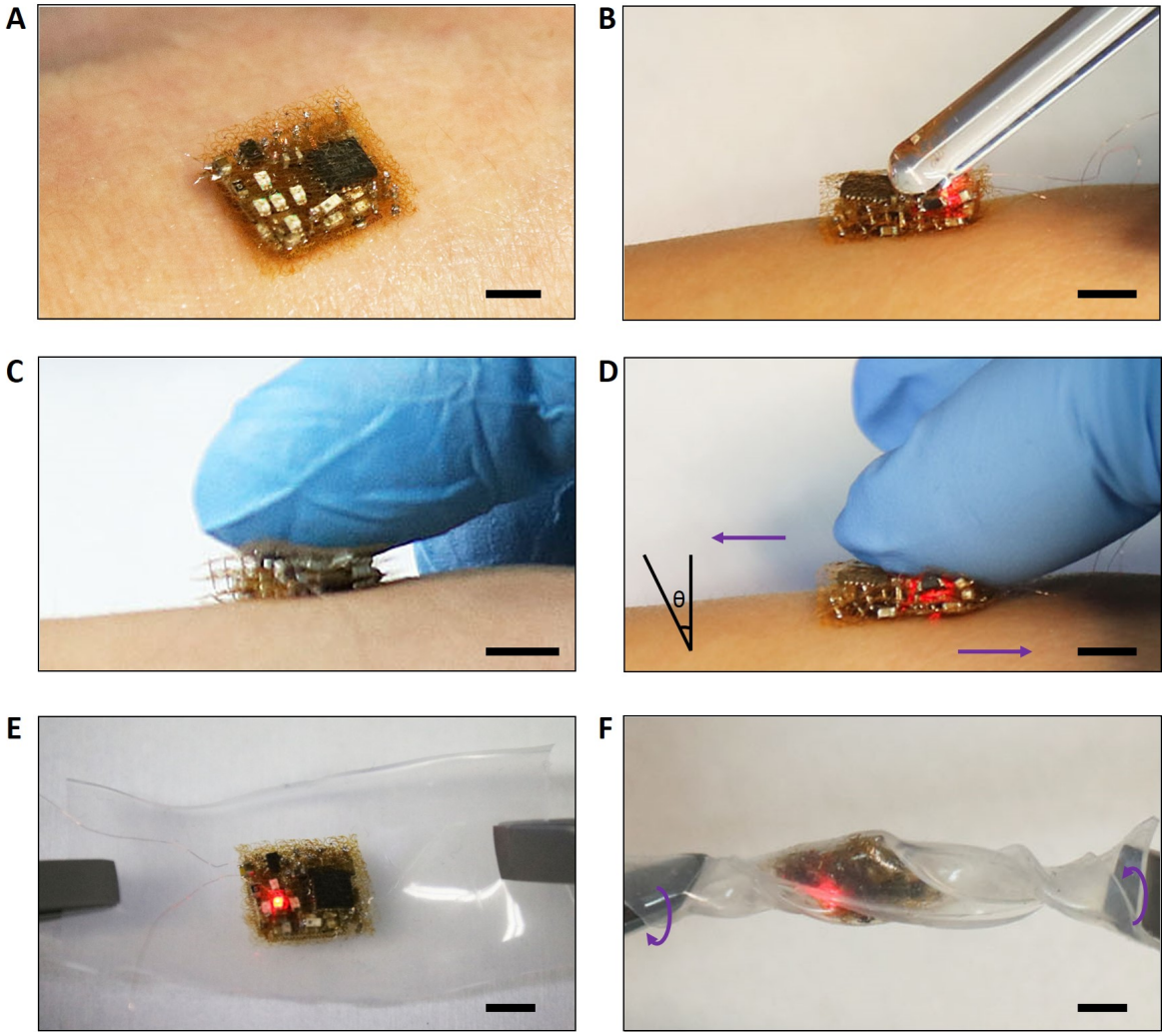

fig. S20. Optical images of the integrated device system mounted on the skin (A), and deformations of the device system when pressing (~ 15%) (B), before (C) and after scratching (~ 32°) (D), before (C) and after twisting (attached on an Ecoflex film that is twisted by ~ 540°) (D). Scale bar 5 mm.

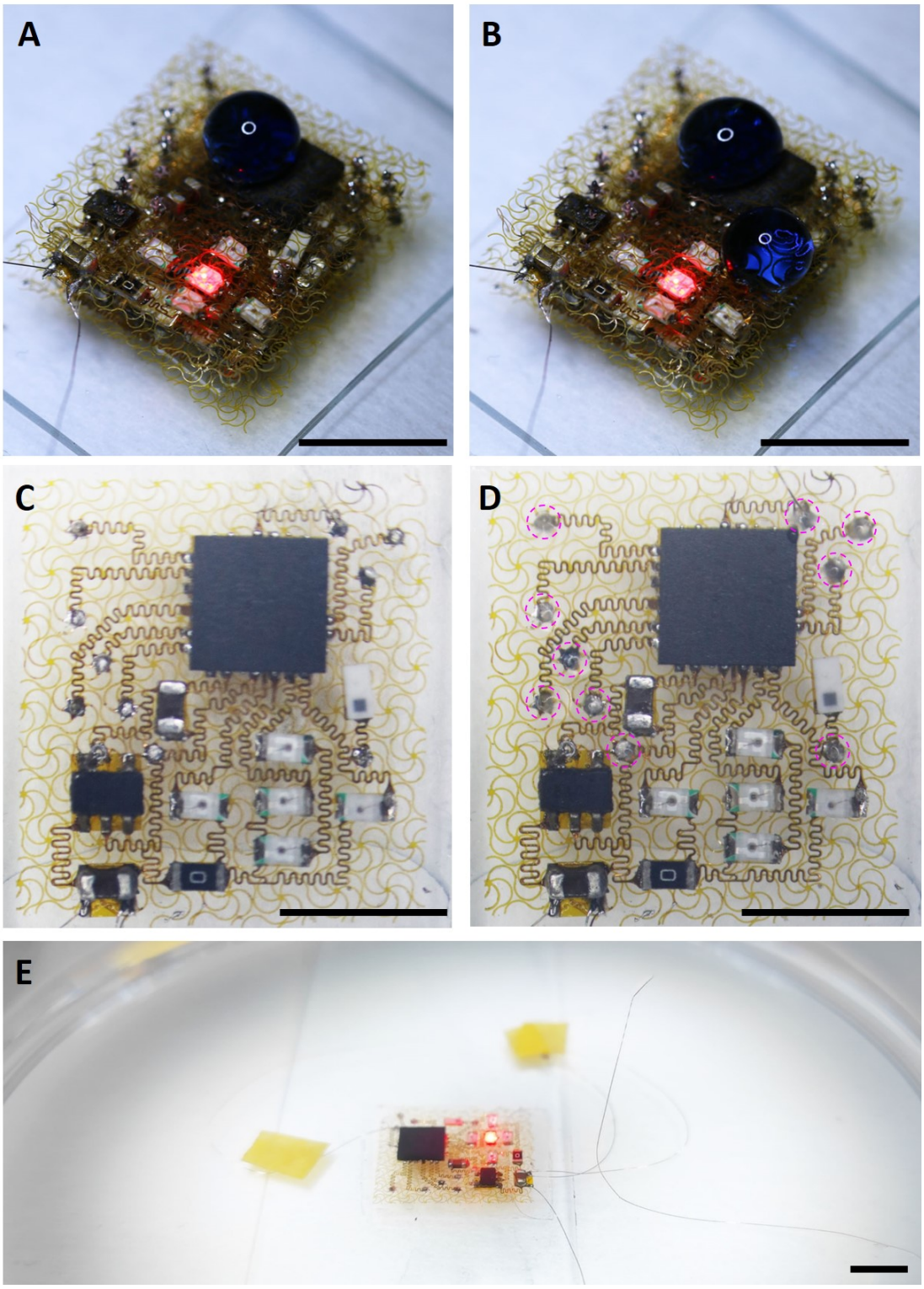

fig. S21. Demonstration of water protection of the integrated system. (**A**)-(**B**) Water droplets on the device system. Images of the connection vias in the 3rd circuit layer before (**C**) and after (**D**) being sealed with silicone rubber (706, RTV, NanDa, China), marked by the dashed circles in (**D**). (**E**) Image of the encapsulated 3rd circuit layer being immersed in deionized water. Scale bars, 5 mm.

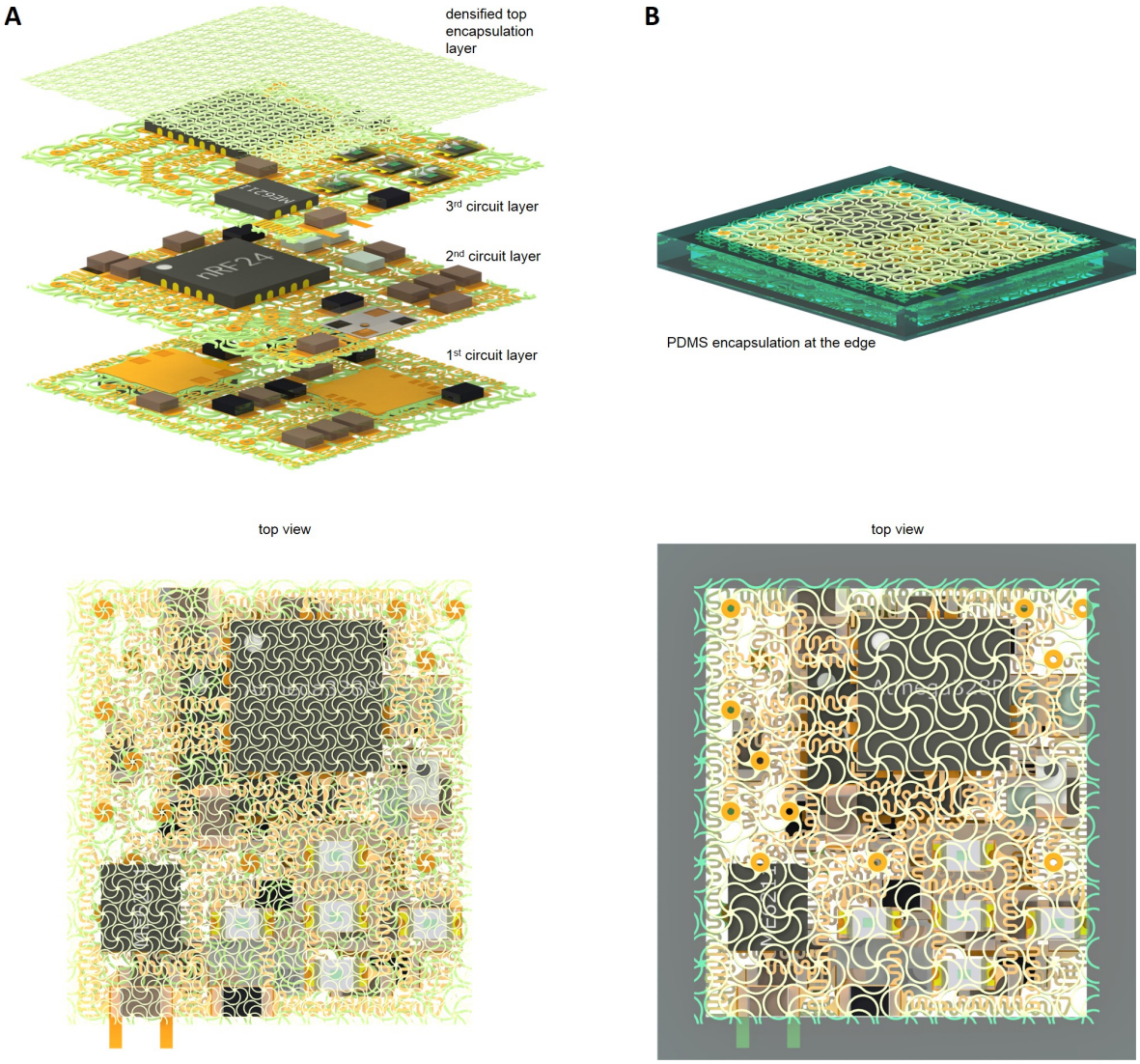

fig. S22. Methods to further improve the protection of electronic devices encapsulated by network material. (A) Exploiting denser network to serve as the top encapsulation layer, and (**B**) encapsulating the edge of the device with soft materials, such as PDMS.

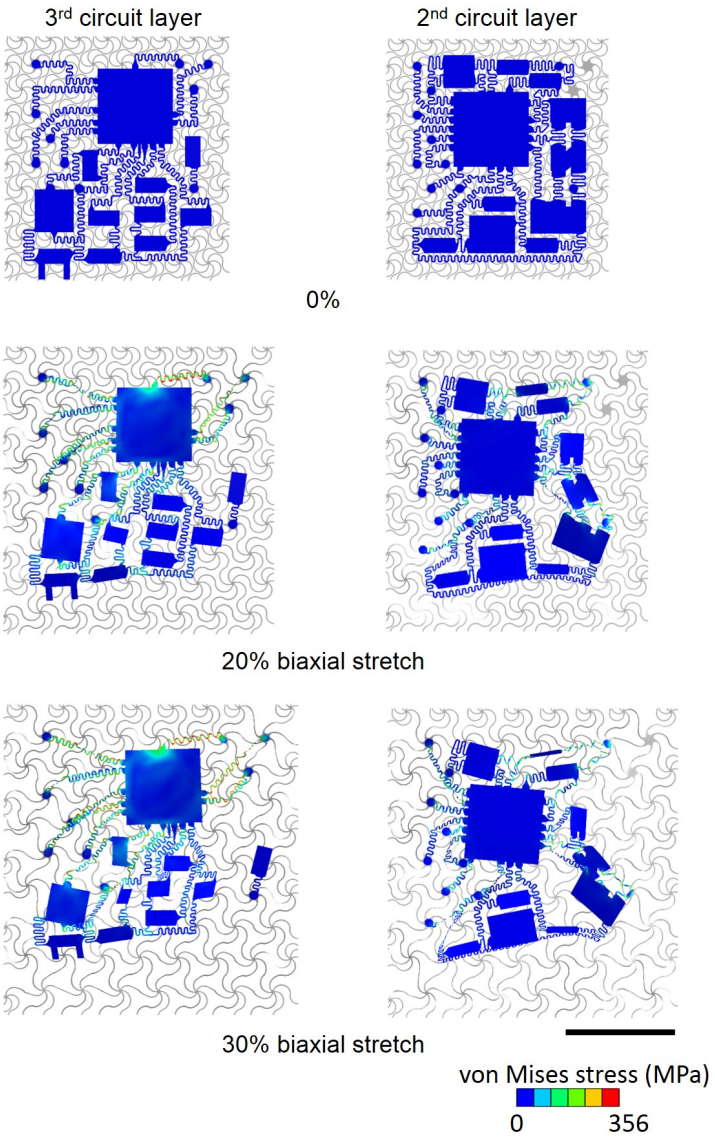

fig. S23. FEA results of the system-level deformations for the 3rd circuit layer and 2nd circuit layer, during different levels of biaxial stretching (0%, 20% and 30%). The color of serpentine interconnects denotes the magnitude of von Mises stress in the metal layer. Scale bars, 5 mm.

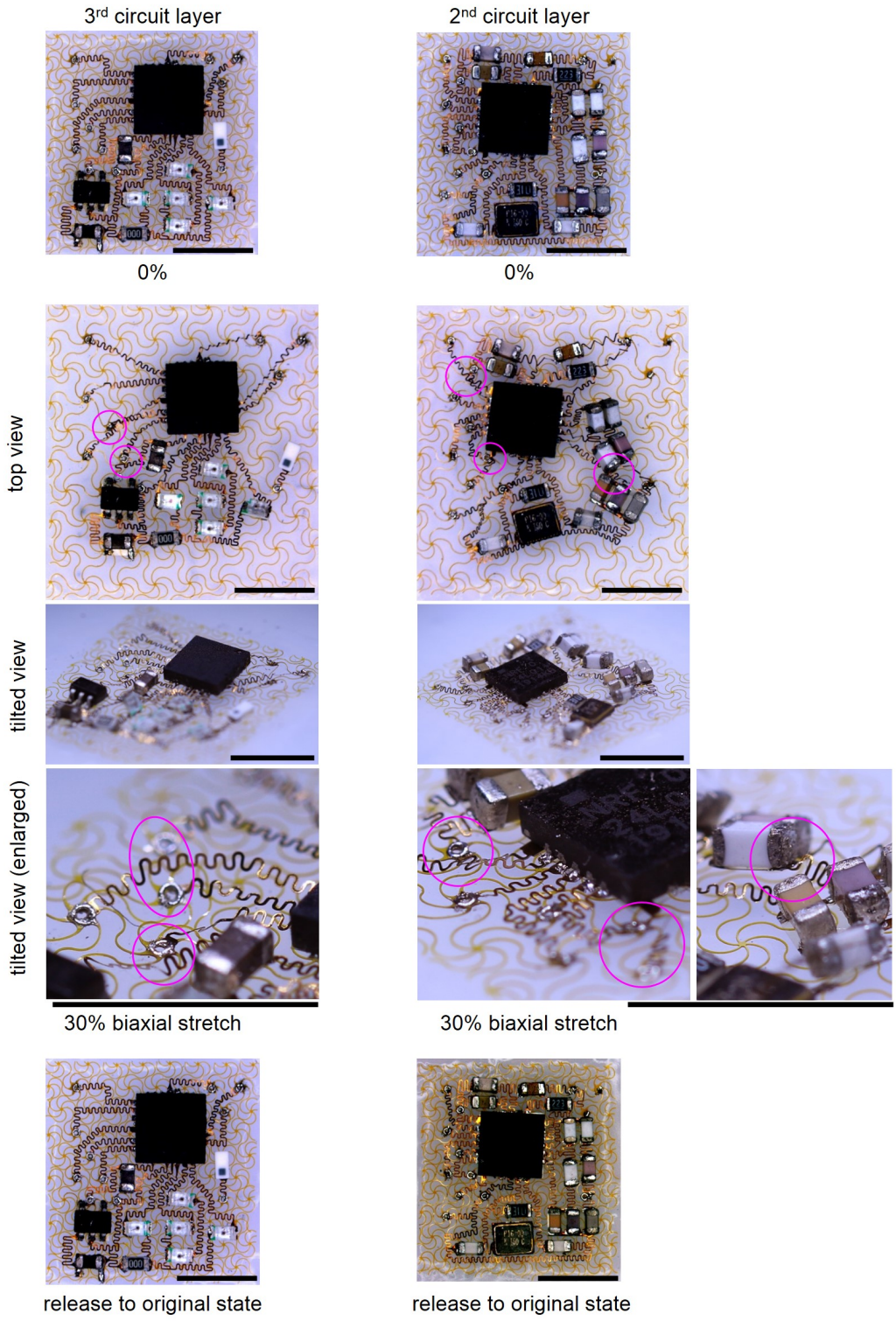

fig. S24. Pictures of the 3rd circuit layer and 2nd circuit layer before loaded and after released. Scale bars, 5 mm.

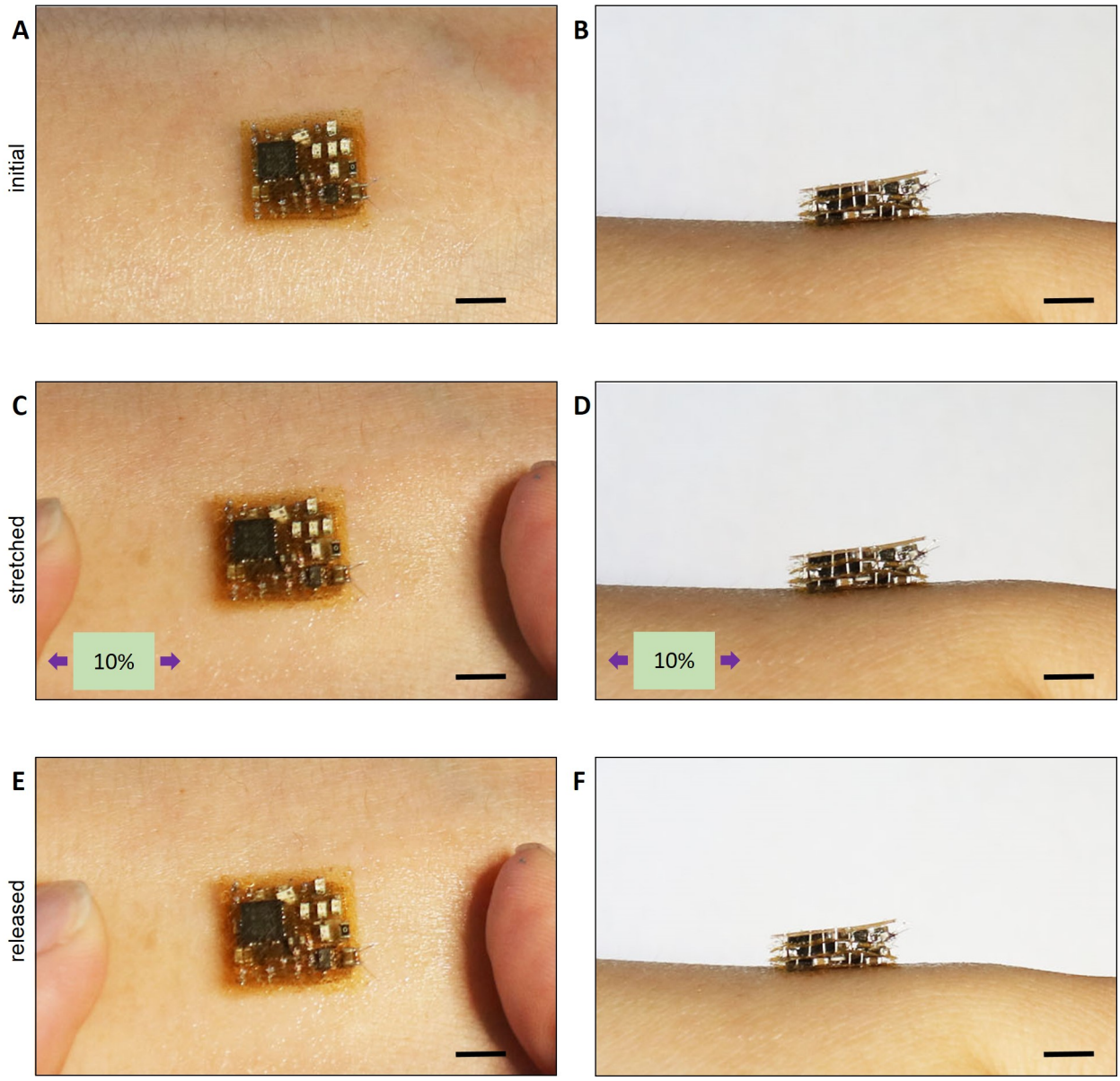

fig. S25. Images of the device mounted on the skin from the top and side views: (A)-(B) Initial state; (C)-(D) Deformed state under 10% uniaxial stretching; and (E)-(F) Released state after 50 cycles of ~10% uniaxial stretching and releasing. Scale bars, 5 mm.

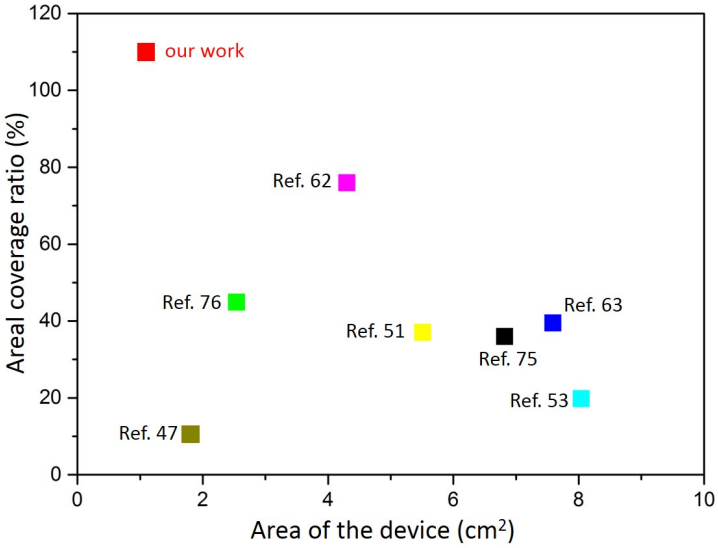

fig. S26. Areal coverage ratio versus the area of the system for representative stretchable skin-integrated electronic devices, including the current work and those reported previously.

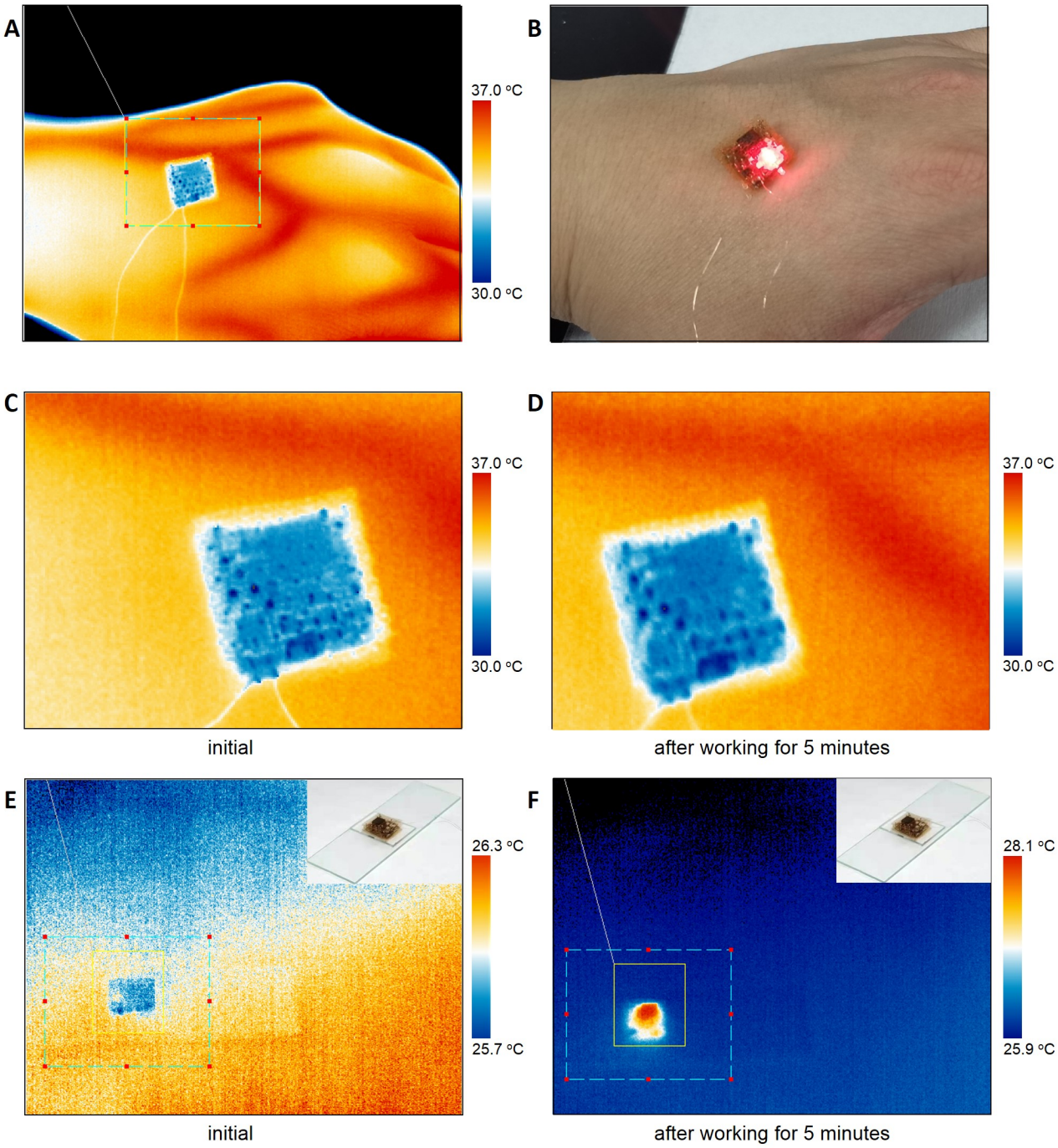

fig. S27. Thermal imaging for the integrated device system. (**A**)-(**B**) Thermal and optical images of the device when mounted on the skin. (**C**) An enlarged view of (**A**) when the system is OFF. (**D**) Thermal image of the device after operation for 5 minutes. The thermal image was captured right after the LED was turned off, as the emitting of LED could disturb the thermal imaging. (**E**)-(**F**) Thermal images of the integrated device system on a PDMS substrate, before and after operation for 5 minutes. A Vario CAM HD camera (thermographic system) was used to capture the temperature distribution.

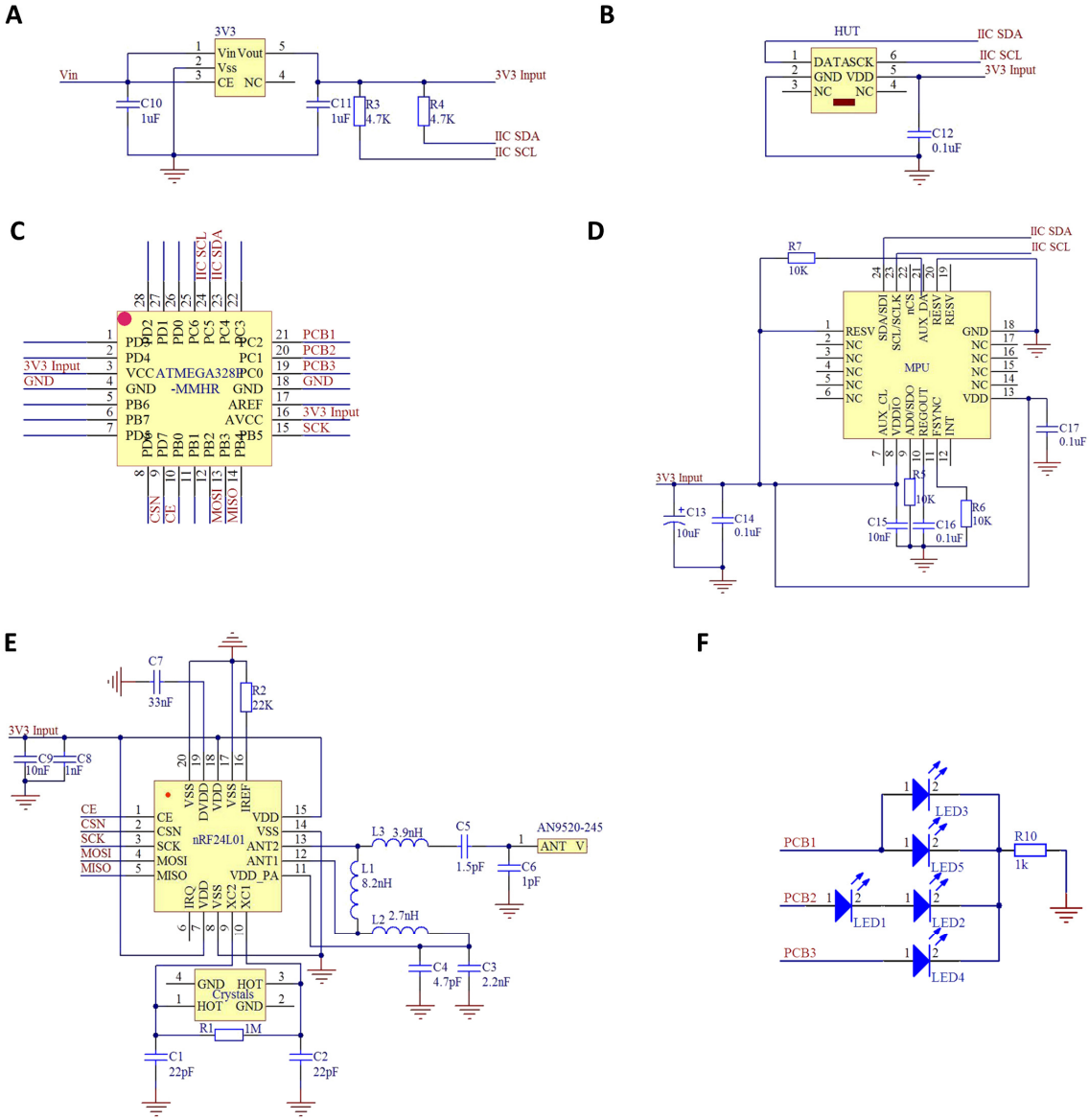

fig. S28. Schematic illustration of the circuit design for the stretchable electronic system based on stacked multilayer network materials. The device encompasses mainly 6 sub-modules: (**A**) 3.3V voltage stabilizing circuit, (**B**) circuit of temperature and humidity sensor, (**C**) micro-controller unit, (**D**) motion detection circuit (namely, gyroscopes, accelerometers and magnetometers, 9 DOF in total), (**E**) 2.4G RF wireless transmission sub-module, and (**F**) LED array for display.

Device No.	Type	Value	Area			Package
			L(mm)	W(mm)	Sum(mm^2)	
1	HTU21D	-	3.1	3.1	9.61	QNF-6
2	MPU9520	-	3.1	3.1	9.61	QNF-24
3	Voltage	-	2.6	2.2	5.72	MSOP-5
4	MCU	-	4.05	4.05	16.4025	QNF-28
5	nRF24	-	4	4	16	QNF-20
6	ANT	-	1.75	0.95	1.6625	0603
7	Crystal	-	2.6	2.1	5.46	-
8-12	LED1-5	-	1.75	0.95	1.6625*5	0603
13, 14	C1, C2	22 pF	1.75	0.95	1.6625*2	0603
15	C3	2.2 nF	1.75	0.95	1.6625	0603
16	C4	4.7 pF	1.75	0.95	1.6625	0603
17	C5	1.5 pF	1.75	0.95	1.6625	0603
18	C6	1 pF	1.75	0.95	1.6625	0603
19	C7	33 nF	1.75	0.95	1.6625	0603
20	C8	1 nF	1.75	0.95	1.6625	0603
21, 22	C9, C15	10 nF	1.75	0.95	1.6625*2	0603
23, 24	C10, C11	1 uF	1.75	0.95	1.6625*2	0603
25,26, 27,28	C12, C14, C16, C17	0.1 uF	1.75	0.95	1.6625*2	0603
29	C13	10 uF	1.75	0.95	1.6625	0603
30	R1	1 MΩ	1.75	0.95	1.6625	0603
31	R2	22 KΩ	1.75	0.95	1.6625	0603
32, 33	R3, R4	4.7 KΩ	1.75	0.95	1.6625*2	0603
34, 35, 36	R5, R6, R7	10 KΩ	1.75	0.95	1.6625*3	0603
37	R9	1 KΩ	1.75	0.95	1.6625*2	0603
38, 39	R01, R02	0 Ω	1.75	0.95	1.6625*2	0603
40	L1	8.2 nH	1.75	0.95	1.6625	0603
41	L2	2.7 nH	1.75	0.95	1.6625	0603
42	L3	3.9 nH	1.75	0.95	1.6625	0603
Total chips in number: 42						
Total areas: 124.315 mm^2						

fig. S29. Material and size information of the individual components used in the stretchable electronic system. There are 42 individual components in total, with an area of 124.315 mm^2.

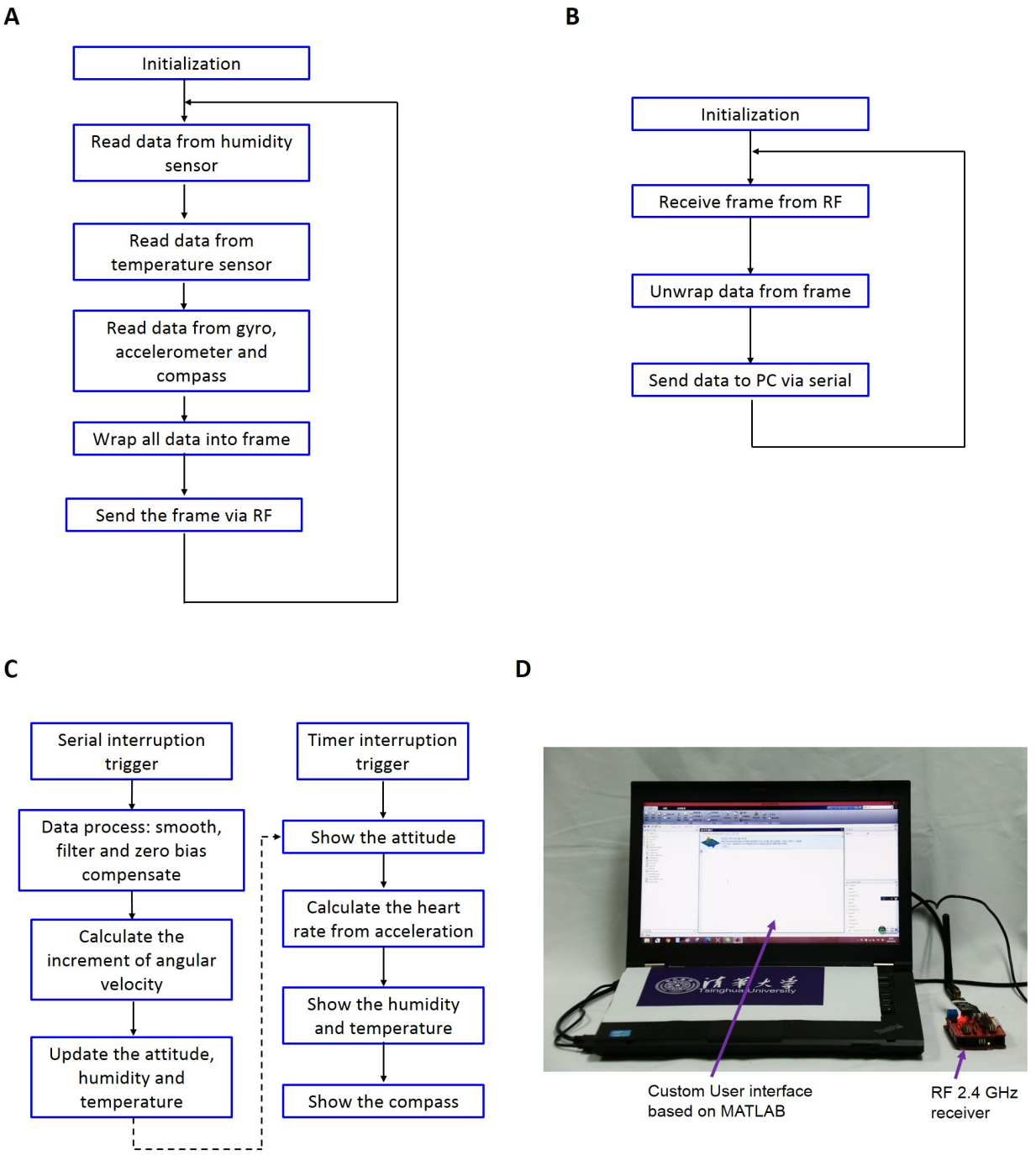

fig. S30. Flow diagram describing the procedure flow chart of the integrated device. (**A**) Flowchart of the onboard system of the integrated device. (**B**) Flowchart of the onboard program of the RF wireless transceivers. (**C**) Flowchart of the real-time data process program on a laptop. (**D**) Image of the system working, with a custom RF 2.4 GHz receiver, and a laptop with a custom interface based on software MATLAB.

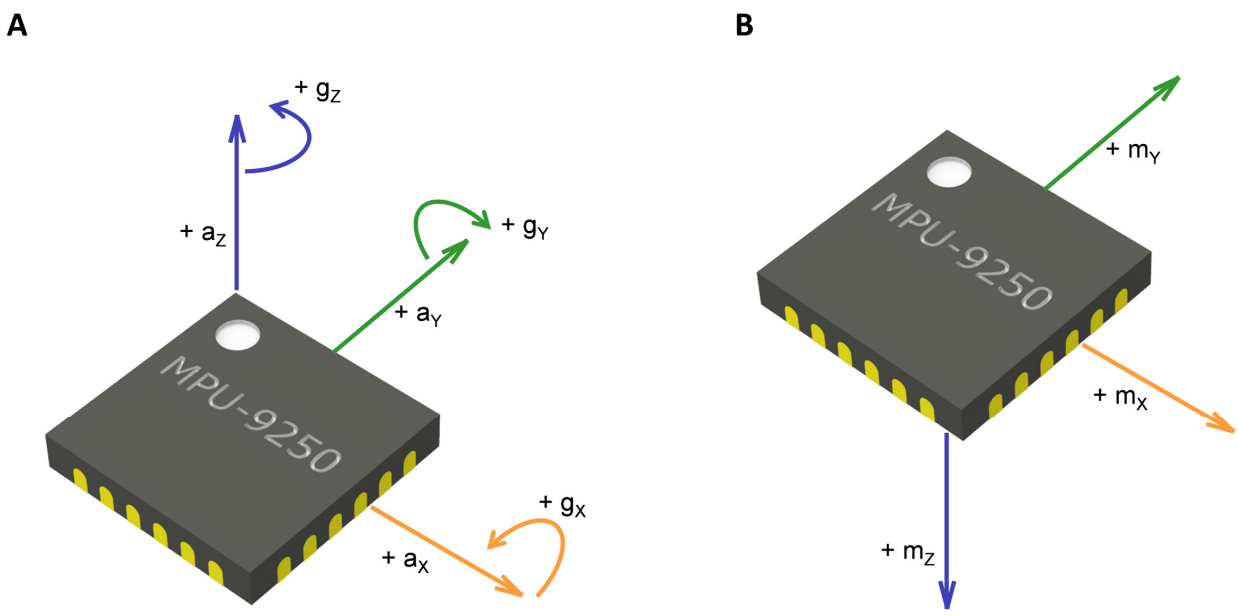

fig. S31. Direction definition of the components of acceleration, angular velocity, and magnetic induction obtained from the MPU-9250 motion-processing unit.

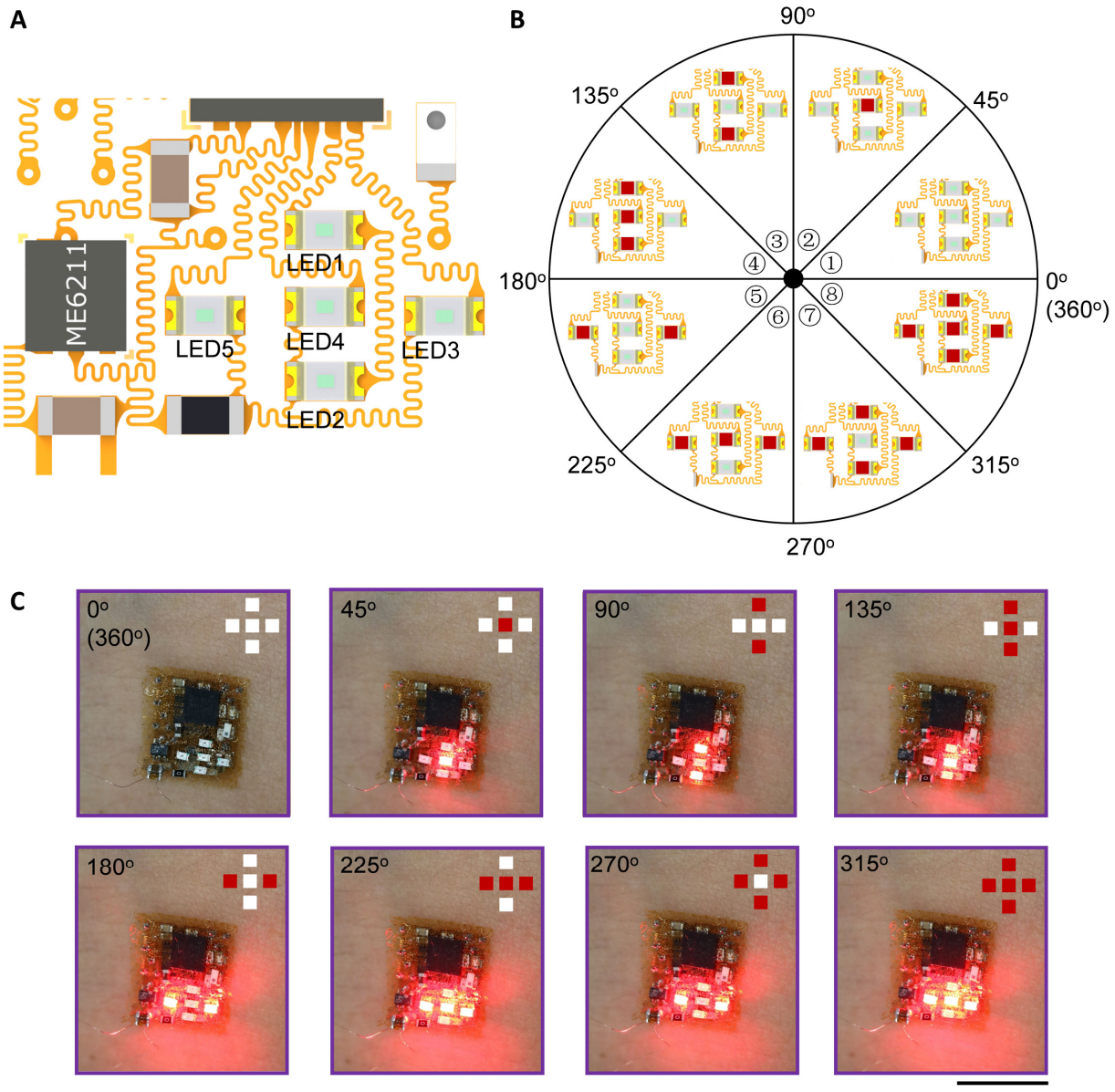

fig. S32. Design of the LED array to serve as an indicator of the orientation angle. (**A**) Illustration of the five LEDs in the array. (**B**) Eight regimes of the orientation angle (from 0° to 360°) and the corresponding state of the LED array. (**C**) Optical images that show the eight lighting modes of the LED array described in (**B**). Scale bar, 1 cm.

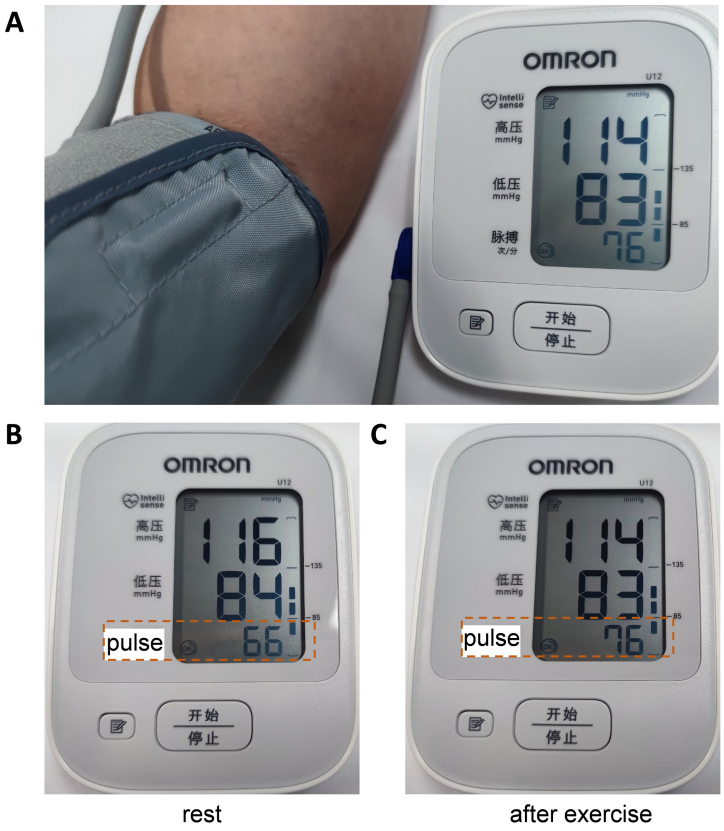

fig. S33. Measurement of the heart rate at rest and after a period of exercise, using a commercial sphygmomanometer.

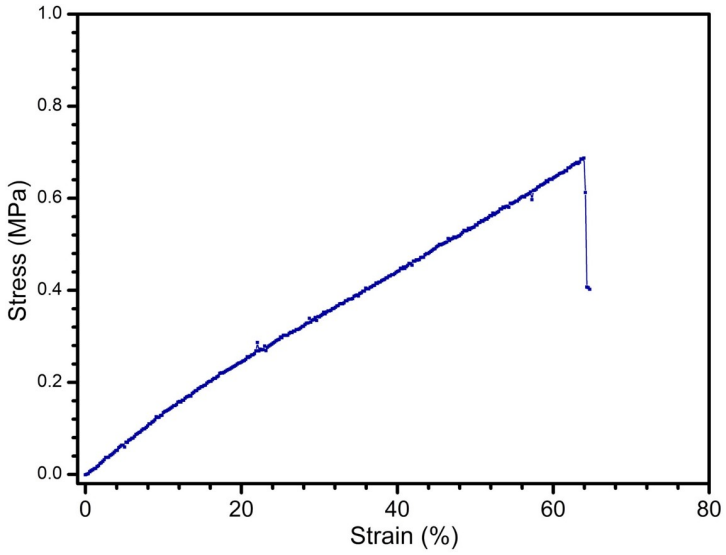

fig. S34. Results of tensile testing for the solidified PDMS used for encapsulation of serpentine interconnects. The sample is measured by a commercial mechanical testing machine, and the elastic modulus of the PDMS is 0.81 MPa.

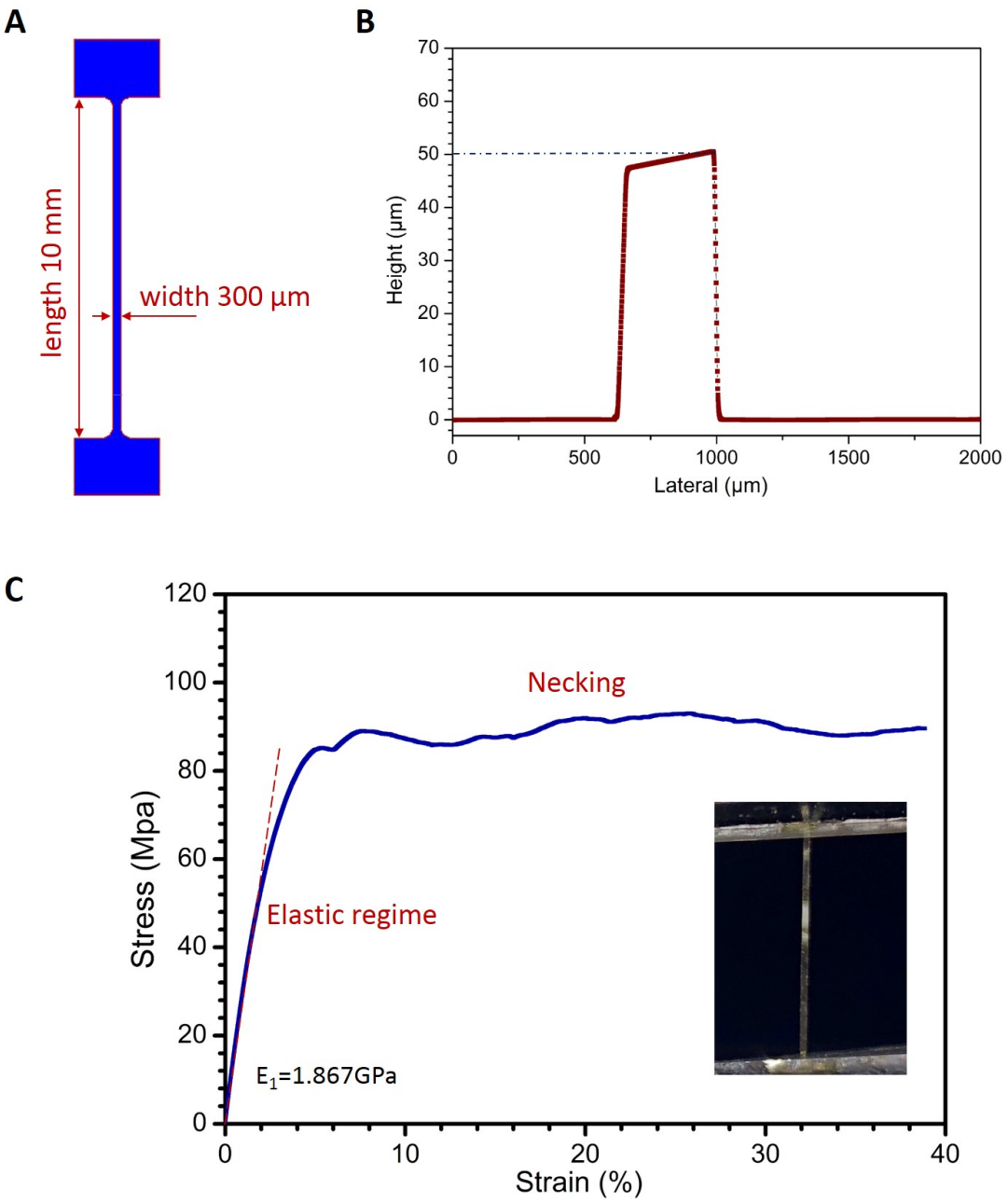

fig. S35. Results of tensile testing for the polyimide material. (**A**) Dimensions of the testing sample, and (**B**) the height profile of the sample (~ 50 µm), measured by a step profiler (Bruker, Dexktak XT). (**C**) Uniaxial stress-strain curves determined from the experiments. The inset is the photo during stretching. According to the results, the elastic modulus of the polyimide material is 1.867 GPa.

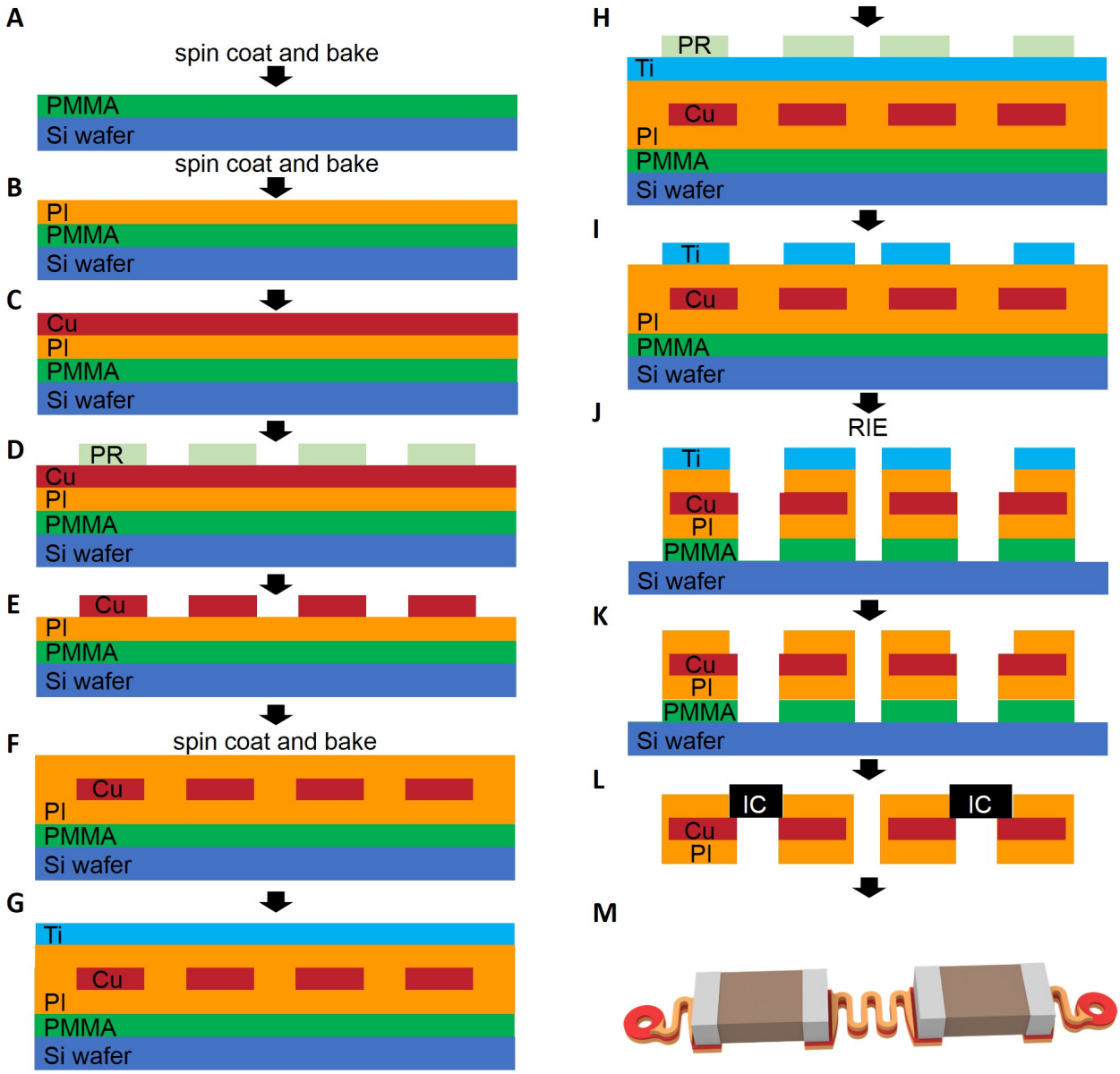

fig. S36. Illustration of the fabrication process for the stretchable serpentine interconnects and integration of the individual components on the top side.

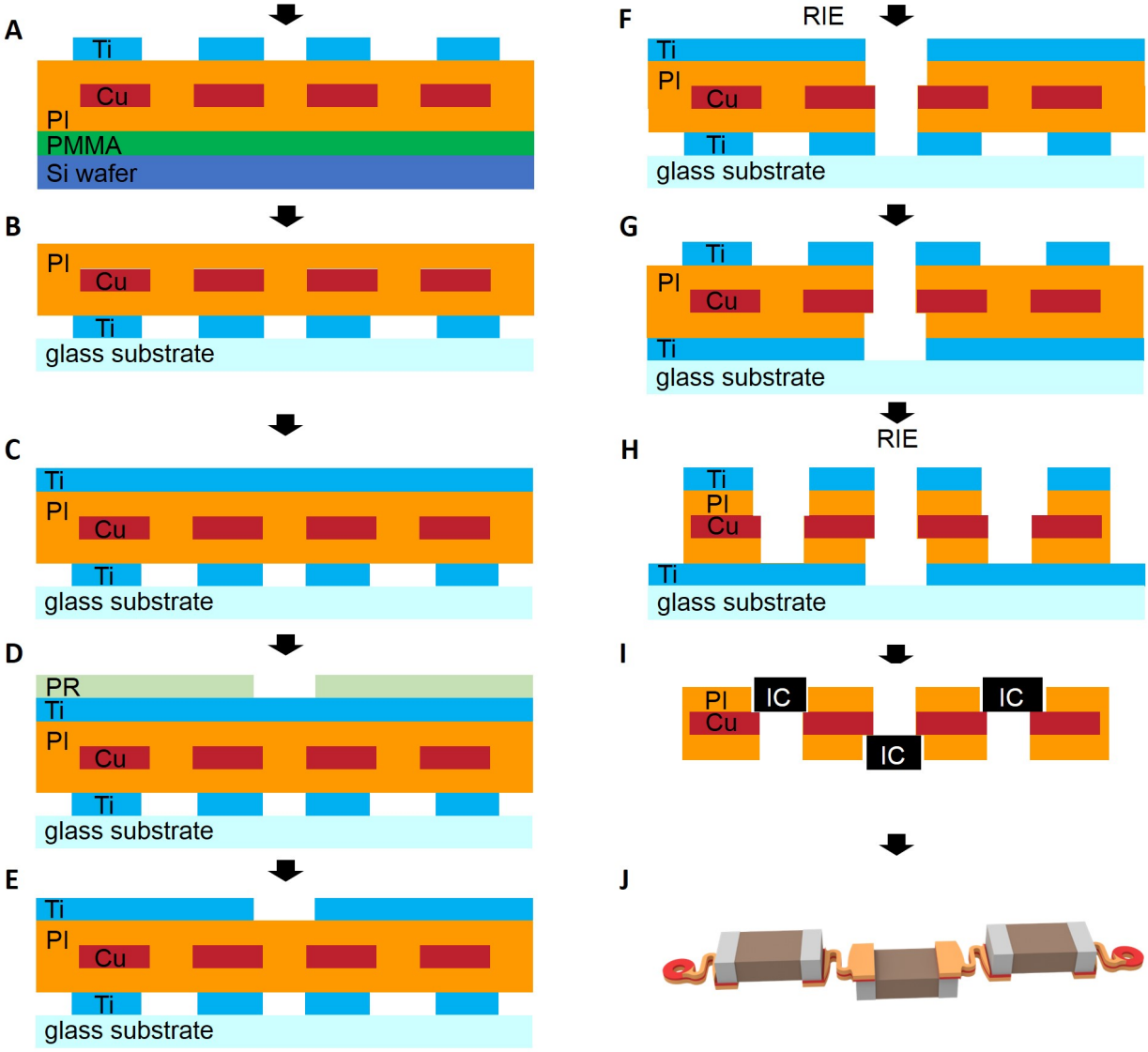

fig. S37. Illustration of the fabrication process for the stretchable serpentine interconnects. Two individual components are integrated on the top side, and the other component is integrated on the back side.

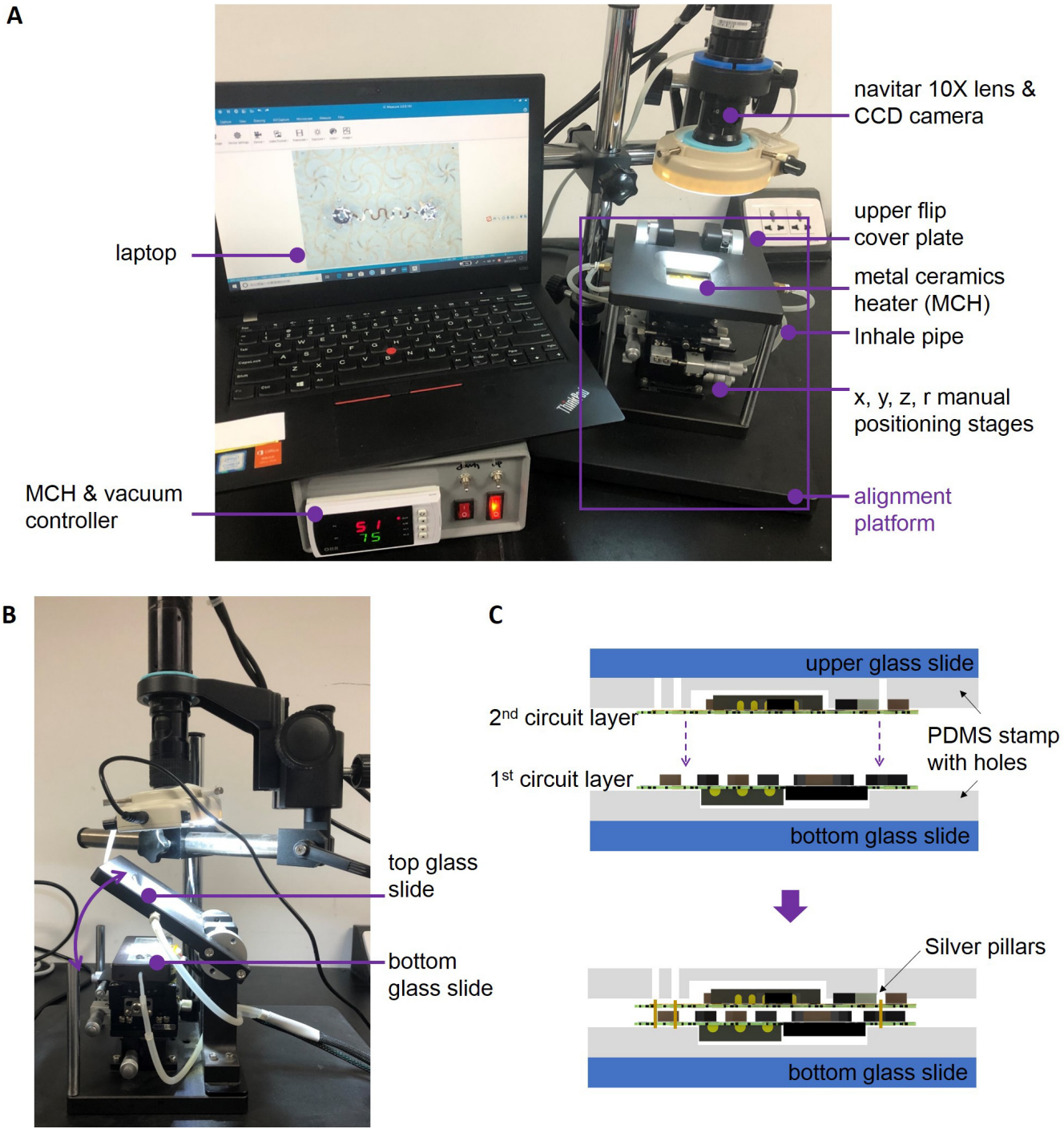

fig. S38. Customized setup for alignment and transfer printing. (**A**) Main part of the alignment system, including a 10 × lens and CCD camera, an alignment stage (with metal ceramics heater for welding, inhale for holding, and 4-axis manual translation stage (*x*, *y*, *z*, and *r*) for positioning). (**B**) Details of the alignment setup, and (**C**) illustration for the process of transfer printing, alignment and welding. During the process of multilayer assembly, the use of PDMS stamp with customized holes can accommodate the height of the electronic components.

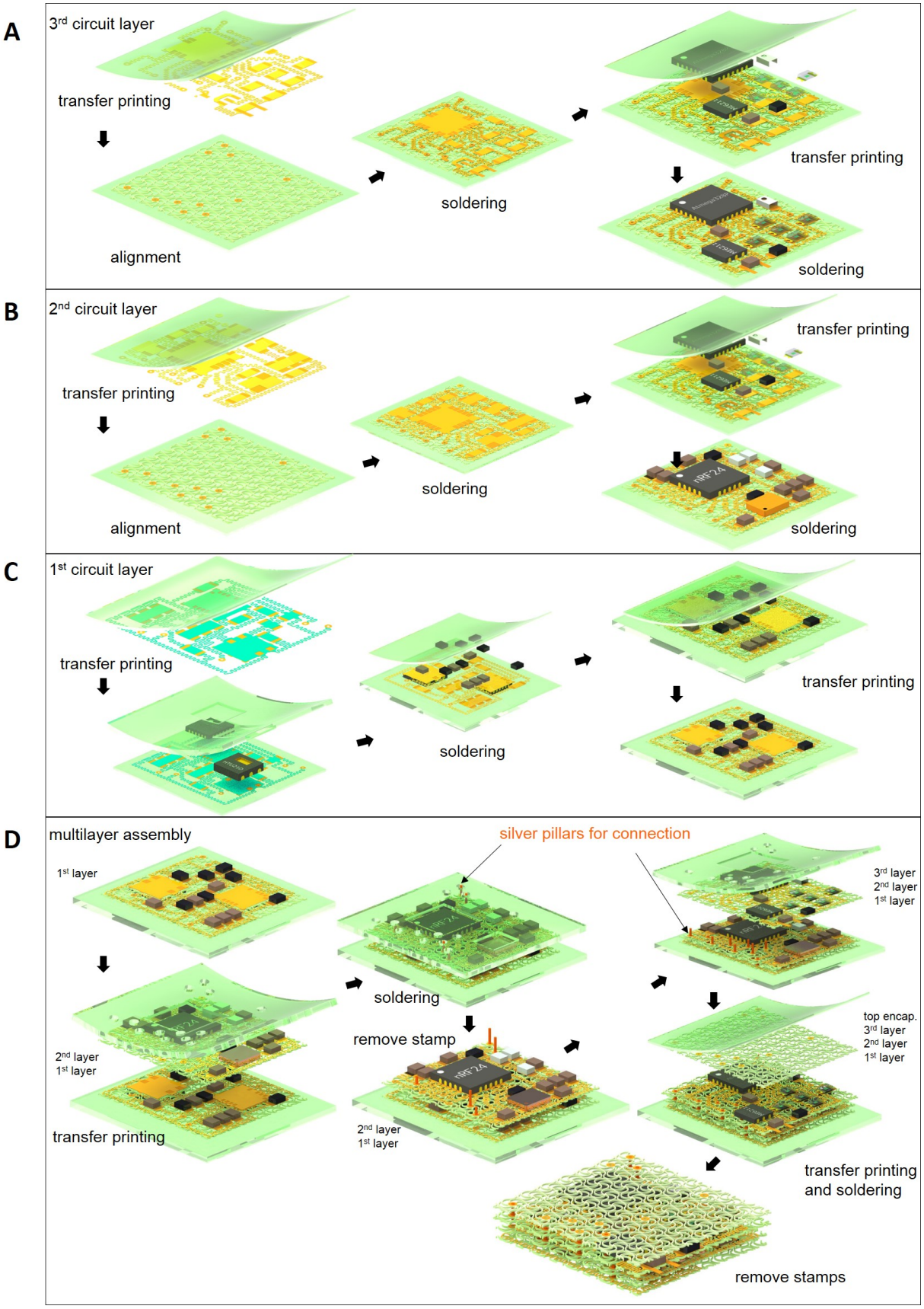

fig. S39. Schematic diagram to show the transfer, assembly and manufacturing process of the device.

Captions of movies

Movie S1. Deformation of serpentine interconnects encapsulated by bilayer network materials in Fig. 1B during uniaxial stretching (to its elastic limit 45%) and unloading.

Movie S2. Deformation of serpentine interconnects encapsulated by PDMS in Fig. 1C during uniaxial stretching (to its elastic limit 6%) and unloading.

Movie S3. Demonstration of 3D motion reconfiguration based on the recorded data of 3-axis acceleration and 3-axis angular velocity from the palm (Fig. 4C).

Movie S4. Demonstration of the somatosensory mouse to play the "*Sokoban pushing box*" game (Fig. 4E).